ACTIVE SURFACE PASSIVATION FOR SWIR INGAAS PHOTODETECTORS

A THESIS SUBMITTED TO
THE GRADUATE SCHOOL OF NATURAL AND APPLIED SCIENCES
OF
MIDDLE EAST TECHNICAL UNIVERSITY

BY

NECATİ IŞIK

IN PARTIAL FULFILLMENT OF THE REQUIREMENTS
FOR
THE DEGREE OF MASTER OF SCIENCE
IN
ELECTRICAL AND ELECTRONICS ENGINEERING

JANUARY 2022

Approval of the thesis:

ACTIVE SURFACE PASSIVATION FOR SWIR INGAAS PHOTODETECTORS

submitted by **NECATİ IŞIK** in partial fulfillment of the requirements for the degree of **Master of Science** i**n Electrical and Electronics Engineering, Middle East Technical University** by,

Prof. Dr. Halil Kalıpçılar
Dean, Graduate School of **Natural and Applied Sciences** _____

Prof. Dr. İlkay Ulusoy
Head of the Department, **Electrical and Electronics Eng.** _____

Assoc. Prof. Dr. Serdar Kocaman
Supervisor, **Electrical and Electronics Eng., METU** _____

Examining Committee Members:

Prof. Dr. Cengiz Beşikci
Electrical and Electronics Eng., METU _____

Assoc. Prof. Dr. Serdar Kocaman
Electrical and Electronics Eng., METU _____

Prof. Dr. Tayfun Akın
Electrical and Electronics Eng., METU _____

Prof. Dr. Barış Bayram
Electrical and Electronics Eng., METU _____

Assoc. Prof. Dr. Dinçer Gökcen
Electrical and Electronics Eng., Hacettepe University _____

Date: 27.01.2022

I hereby declare that all information in this document has been obtained and presented in accordance with academic rules and ethical conduct. I also declare that, as required by these rules and conduct, I have fully cited and referenced all material and results that are not original to this work.

Name, Surname: Necati Işık

Signature:

ABSTRACT

ACTIVE SURFACE PASSIVATION FOR SWIR INGAAS PHOTODETECTORS

Işık, Necati
Master of Science, Electrical and Electronics Engineering
Supervisor: Assoc. Prof. Dr. Serdar Kocaman

January 2022, 75 pages

This thesis work offers a new method for decreasing surface leakage current in infrared photodetector technology. This method involves suppressing the surface dark current by utilizing a constant E-field on the surface of the photodetector. By interrupting the channel formation on the surface, a significant improvement in the generation recombination (GR) dark current component is observed. Relatively minor improvements on differential resistance and the shunt component of the dark current are noted. Lattice-matched short-wave infrared (SWIR) Indium-Gallium-Arsenide (InGaAs) grown on Indium-Phosphide (InP) sample with a cut-off wavelength of 1.69 μm is processed with mesa etching of 30 μm pixel pitch to verify this claim. The proper operation of the photodetector is verified using responsivity measurements. Reported total dark currents reduced from 195 pA to 70 pA per pixel with -0.1 V bias at 300 K temperature and 175 pA to 39 pA per pixel at 290 K. Using the dark current modeling, determined GR currents observed to be decreased by more than 90%. The feasibility of this structure is discussed whether it is possible to be implemented on focal plane arrays (FPAs).

Keywords: Active Surface Passivation, SWIR InGaAs, Surface Current Suppression, GR Current Suppression

ÖZ

KISA-DALGA KIZILÖTESİ İNDİYUM-GALYUM-ARSENİK DİZİNLERİ İÇİN GELİŞTİRİLEN AKTİF YÜZEY PASİVASYONU

Işık, Necati
Yüksek Lisans, Elektrik ve Elektronik Mühendisliği
Tez Yöneticisi: Doç. Dr. Serdar Kocaman

Ocak 2022, 75 sayfa

Bu tez çalışması, kızılötesi foton detektörü teknolojileri kapsamındaki performans parametrelerinden birisi olan, yüzey pasivasyonun geliştirilmesi ve yüzey akımının düşürülmesini sağlayacak özgün bir yöntem sunmaktadır. Bu yöntem yüzeye sabit elektriksel alan uygulamak suretiyle yüzey şartlarının değiştirilmesi üzerine dayanmaktadır. Yüzeyde oluşan akım kanalı sekteye uğratılarak, üretim-yeniden birleşim (GR) karanlık akım bileşeninde önemli ölçüde iyileşme gözlenmiştir. Bununla birlikte, parallel devre direncinden kaynaklı oluşan karanlık akımda ve diferansiyel direnç değerlerinde iyileşmeler kaydedilmiştir. Bu tez dahilinde önerilen yapının doğrulamasının yapılabilmesi için İndiyum-Fosfat (InP) alt taban üzerine örgü uyumlu İndiyum-Gallium-Arsenik (InGaAs) malzemesi büyütülmüş bir malzeme kullanılmıştır. Bu malzemenin, kısa-dalga kızılötesi (SWIR) aralığı olarak nitelendirilen 1.69 mikrometre uzunluğundaki kesim dalga boyu tepkisellik ölçümleri ile doğrulanmıştır. 30 mikrometre adım uzunluğuna sahip pikseller ıslak aşındırma yöntemi kullanılarak üretilmiştir. 300 Kelvin sıcaklığında, negatif 0.1 eğimleme voltajı uygulanarak yapılan karanlık ölçüm sonuçlarında; piksel başına karanlık akımın 195 piko-amperden 70 piko-amper mertebesinde düştüğü, 290 Kelvin sıcaklığında yapılan ölçümlerde ise 175 piko-amperden 39 piko-amper seviyesine düştüğü gözlenmiştir. Karanlık akım modellemeleri sonucunda GR

karanlık akımında %90’dan fazla oranda iyileşme olduğu kaydedilmiştir. Sunulan yöntemin, odak düzlem matrislerine (FPA) uygulanabilirliği üzerine tartışmalara yer verilmiştir.

Anahtar Kelimeler: Aktif Yüzel Pasivasyonu, SWIR InGaAs, Yüzey Akımı Baskılama, GR Akımı Baskılama

An idea is a fantasy to a single mind, revolution to kindred ears, standard to the masses.

To my family

ACKNOWLEDGMENTS

First and foremost, I would like to express my deepest gratitude to my supervisor Assoc. Prof. Dr. Serdar Kocaman for his guidance, advice and criticism throughout this research. Certainly, I would not survive without his support and encouragements throughout this thesis.

I would like to thank Prof. Dr. Cengiz Beşikci for his valuable comments and feedbacks as well as allowing me to do my research in such a great laboratory.

I would like to thank Prof. Dr. Tayfun Akın, Prof. Dr. Barış Bayram, Assoc. Prof. Dr. Dinçer Gökcen for their valuable comments and being on my thesis committee.

I would like to thank Alper Şahin for his help with the responsivity measurements and valuable discussions regarding the fabrication steps.

I would like to thank Veysel Balcı, Musa Selim Gül and Halil İbrahim Binici for their friendship, support and discussions.

I would like to thank all of the other members of ODTU-KANAL.

TABLE OF CONTENTS

ABSTRACT v

ÖZ vii

ACKNOWLEDGMENTS x

TABLE OF CONTENTS xi

LIST OF FIGURES xiii

LIST OF TABLES xvi

LIST OF ABBREVIATIONS xvii

1 INTRODUCTION 1

1.1 Basic Concepts of Infrared 2

1.2 Properties and Figures of Merit for Infrared Detectors 11

1.2.1 Dark Current of a Photovoltaic Detector 11

1.2.2 Quantum Efficiency and Responsivity 13

1.2.3 Various Noise Mechanisms 16

1.3 Noise Equivalent Power and Specific Detectivity 19

1.4 Noise Equivalent Temperature Difference 20

1.5 Noise Equivalent Irradiance 21

2 BRIEF SUMMARY OF PHOTOVOLTAIC SWIR TECHNOLOGIES 23

2.1 Various Applications for SWIR Photodetectors 23

2.2 Common SWIR Photovoltaic Detectors 25

3 FABRICATION AND CHARACTERIZATION OF InGaAs/InP SWIR INFRARED TEST DETECTOR WITH ACTIVE SURFACE PASSIVATION ... 33

3.1 A Discussion Regarding the Surface Recombination and Fixed Charges ... 33

3.2 Fabrication of the Test Detector 37
3.2.1 Basics of Molecular Beam Epitaxy 38
3.2.2 Processing of Test Detector 40
3.3 Test Detector Characterization and Modelling 46
3.3.1 Responsivity and Quantum Efficiency Measurement 47
3.3.2 Dark Current Measurements and Modelling 49
3.3.3 Differential Resistance and Shunt Resistance 57
3.3.4 Specific Detectivity and Effective GR Lifetime 62
4 CONCLUSION 65
REFERENCES 69

LIST OF FIGURES

FIGURES

Figure 1.1. Theoretically expected spectral radiant exitance of black bodies with various temperatures vs. wavelength. The given plot is formed by sweeping the wavelength and the designated temperatures in equation 1.7. 5
Figure 1.2. The transmittance of the atmosphere for infrared spectrum (redrawn after [9]). 8
Figure 1.3. Spectral radiance at night due to night glow and different moon conditions (redrawn after [10]). 10
Figure 1.4. Ideal responsivity versus energy gap and wavelength (redrawn after [11]). 15
Figure 1.5. Equivalent circuits for Johnson-Nyquist noise. 16
Figure 1.6. A typical frequency spectrum of a noise current with respect to measured frequency. 18
Figure 1.7. Spectral specific detectivity of a photon detector. 20
Figure 2.1. Band structure in energy-momentum space. **(A)** Typical direct bandgap semiconductor. **(B)** Band diagram of Ge, electrons occupy the indirect L-valley. **(C)** Inducing strain to Ge or alloying with Sn decreases the bandgap, resulting in a population increase in Γ-valley (redrawn after [19]). 26
Figure 2.2. Energy gap and the cut-off wavelength of $Hg_{1-x}Cd_xTe$ with corresponding lattice constant and mole fraction (x) at 77 K. 27
Figure 2.3. Typical SWIR planar InGaAs/InP structure (redrawn after [42]). 30
Figure 2.4. Mesa type SWIR InGaAs/InP structure. 31
Figure 3.1. Surface state energy level below the mid-gap for an n-type semiconductor. 34
Figure 3.2. Device resistance vs. surface charge densities for various bulk carrier densities of a photoconductor. Derived using equation 3.3. (Used parameters l = 30 μm, w = 30 μm, d = 3 μm. N_b denotes bulk carrier density, N_s denotes surface charge

density. The other required parameters are used given in table 2.1.) A similar study for an MCT photoconductive detector is published in ref.: [21]. 36
Figure 3.3. Simplified sketches of (A) metal oxide semiconductor (MOS) and (B) suggested structure..... 37
Figure 3.4. A representative sketch of the growth chamber of the MBE reactor.... 39
Figure 3.5. MBE grown epilayer of the photodetector. 40
Figure 3.6. μPG 501 – Direct Writer system made by Heidelberg Instruments. METU - Quantum Devices and Nanophotonics Research Laboratory..... 41
Figure 3.7. Simplified process flow of the fabrication. Given *colors* representing *gold*: contacts, *violet*: passivation, *brown*: substrate, *blue/green*: epilayers. 42
Figure 3.8. Scanning-electron-microscope (SEM) image of a sample after the mesa etching..... 43
Figure 3.9. Detector image under an optical microscope with 100x zoom. Metal paths of surface-gate contact (yellow) and p-contact (red) are marked with dashed lines. 44
Figure 3.10. The last metal mask was used in the SWIR photodetector process. ... 45
Figure 3.11. Snapshot of the final detector under an optical microscope with 5x zoom..... 46
Figure 3.12. Responsivity measurement setup (top) and representative schematic (bottom)..... 47
Figure 3.13. The responsivity of the photodetector. The sample is illuminated from the backside. InP substrate with a thickness of 800 μm was not thinned down. Calibrated InAs detector is used as a reference detector. 49
Figure 3.14. Dark current IV graph for various surface-gate biases with pn-junction terminal biasing voltage swept from -1 to 0.6 V at 300 K. 50
Figure 3.15. Dark current IV graph for various surface-gate biases with pn-junction terminal biasing voltage swept from -1 to 0.4 V at mild room temperature. 51
Figure 3.16. IV modeling of the experimental result for zero surface-gate biasing case at 300 K temperature. 53

Figure 3.17. IV modeling of the experimental result for 54 V/μm surface-gate biasing at 300 K temperature..... 54
Figure 3.18. IV modeling of the experimental result for zero surface-gate biasing case at mild room temperature. 55
Figure 3.19. IV modeling of the experimental result for 30 V/μm surface-gate biasing at mild room temperature. 56
Figure 3.20. Calculated dynamic resistance with given applied surface-gate biasing at 300 K temperature..... 58
Figure 3.21. Calculated dynamic resistance with given applied surface-gate biasing at mild room temperature. 59
Figure 3.22. Calculated shunt resistances (*black box*) and fitting (*red line*) for various surface-gate biasing at 300 K temperature. 61
Figure 3.23. Calculated effective GR lifetime for various applied surface-gate voltages at 300 K. 63

LIST OF TABLES

TABLES

Table 2.1 $In_{0.53}Ga_{0.47}As$ Material Parameters at 300 K 29
Table 2.2 InP Material Parameters at 300 K 30
Table 2.3 State-of-the-art performance comparison of planar type InGaAs/InP SWIR photodetectors..... 32
Table 3.1 Experimentally calculated figure of merits at mild room temperature. It is calculated with a peak responsivity of 0.9 A/W at 1630 nm wavelength. 62
Table 3.2 Details of the fitting parameters for the measurement made at 300 K temperature. (C1: C_{diff}, C2: $C_{g\text{-}r}$, C3: C_{shunt} denoted by equations 3.13-15.)..... 64

LIST OF ABBREVIATIONS

GR	Generation - Recombination
SWIR	Short Wave Infrared
NIR	Near-Infrared
InGaAs	Indium-Gallium-Arsenide
InP	Indium-Phosphide
MCT	Mercury-Cadmium-Telluride
GaAs	Gallium-Arsenide
Si	Silicon
Ge	Germanium
Sn	Tin
FPA	Focal Plane Array
PD	Photodetector
LIDAR	Light Detection and Ranging
f/#	F-number
SNR or **S/N**	Signal-to-Noise-Ratio
QE	Quantum Efficiency
MBE	Molecular Beam Epitaxy
MOS	Metal-Oxide-Semiconductor
MOSFET	Metal-Oxide-Semiconductor Field Effect Transistor

CHAPTER 1

INTRODUCTION

Infrared (IR) is electromagnetic radiation, also referred to as infrared light. It corresponds to an electromagnetic spectrum with wavelengths longer than visible light and shorter than microwaves. Visible light is considered 400-700 nm wavelength range; therefore, the IR spectrum contains the region of wavelengths from 700 nm up to 1 mm. Short-wave-infrared (SWIR) is classified with wavelengths of 1 to 3 μm.

The adoption of semiconductor-based technologies started a new technological era. Nowadays, Silicon (Si) based technologies are powered up almost every technological device that uses electricity. Similarly, compound semiconductors and their applications mean a lot in this technological revolution. They are perhaps a little hidden to the common eye even though they are used in many areas, from the backbone of the communication infrastructure to tactical military equipment and deep space exploration. As compound semiconductor technologies got mature, compound semiconductors now offer a viable solution for the industry and the consumer electronics market, such as light detection and ranging (LIDAR) scanners. Moreover, LIDARs operating in the near-infrared (NIR) and SWIR bands are being used to develop self-driving cars, although argued to be not a cost-effective solution at the moment [2].

Mature IR semiconductor photodetectors (PD) proved to be highly effective, especially in the fields where the ultimate performance matters [3]. Nevertheless, there still exist many challenges to push the performance further, as most of the IR PDs require to be intensely-cooled for proper operation, which also drives the cost and power consumptions higher. This thesis offers a new approach for decreasing

the surface leakage current of the IR PDs, which is an important parameter determining the performance of the photodetector. 30-μm pitched mesa etched, SWIR Indium-Gallium-Arsenide (InGaAs)/Indium-Phosphide (InP) test detector was fabricated for this purpose.

This first chapter covers the fundamental concepts of infrared physics. First is the infrared discovery, then the blackbody theory is explained within the thermodynamics perspective. The infrared band formation is expressed with the natural properties of the atmosphere, and commonly used figures of merit are discussed with their limitations.

In Chapter 2, photovoltaic SWIR technology is investigated briefly, and selected InGaAs parameters are given for calculations.

In Chapter 3, the details of the fabrication processes are given. The methodology and experimental results are stated, and the results are discussed with the theoretical expectations. Background information about surface passivation is given as a discussion, and the suggested technique is explained in this chapter.

In Chapter 4, the conclusion of this thesis is addressed. The feasibility of the proposed structure applicability to a focal-plane array (FPA) level is analyzed.

1.1 Basic Concepts of Infrared

The English astronomer William Herschel first discovered IR radiation by letting sunlight pass through a prism to a thermometer. Even beyond the visible spectrum, he noticed a temperature change. He concluded that an invisible light must be exciting the thermometer [4].

Gustav Kirchoff introduced the term blackbody in 1860. The term blackbody radiation is also referred to as thermal radiation. According to the second law of thermodynamics, a net flow of heat incoming from an object should exist.

Furthermore, the total energy should be conserved according to the first law of thermodynamics. Thus, for an object at equilibrium with the surroundings:

$$\phi_{inc} = \phi_{absorbed} + \phi_{transmitted} + \phi_{reflected}, \quad (1.1)$$

ϕ_{inc} is the total incident flux on the blackbody. $\phi_{absorbed}$, $\phi_{transmitted}$, $\phi_{reflected}$ are the absorbed, transmitted, and reflected portion of the incident flux, respectively. Dividing the above equation by ϕ_{inc} yields to:

$$1 = \alpha + \tau + \rho, \quad (1.2)$$

α, τ, ρ are absorbance, transmittance, and reflectance. One of the implications of equation 1.2; say for a perfectly opaque body with no transmittance ($\tau = 0$), the incoming radiation is either absorbed or reflected, means that:

$$\alpha = 1 - \rho, \quad (1.3)$$

which also indicates opaque surfaces with low reflectance are also good absorbers. Kirchoff stated that a perfect black body with no transmittance and no reflectance ($\tau = \rho = 0$) absorbing all the incident radiation should emit incident radiation back in order to remain in thermal equilibrium. In other words, a perfect blackbody with an infinitely thin surface layer, no reflection or scattering that absorbs all the radiation falling on, must emit all the radiation back to stay in equilibrium. The radiation mechanism should behave with Lambert's cosine law [5]. Otherwise, it would mean that the blackbody should reach higher and higher temperatures in time, which means never reaching an equilibrium point.

Max Planck argued that the perfect blackbodies do not occur in physical reality stating that they are 'theoretical fictions' [6]. For the cases of the non-perfect black body (means $\tau \neq \rho \neq 0$), a blackbody (or sometimes referred to as gray body) absorbs the portion of the incident radiation and then emits less radiation to stay in the thermal equilibrium point, which means:

$$E = \varepsilon M, \quad (1.4)$$

E, ε, M are emittance, emissivity, and exitance, respectively. Emissivity is a parameter between 0 and 1; as the emissivity of the black body gets close to 1, it gets closer to the perfect black body condition, which Gustav Kirchoff explained. Aside from the perfect black body discussions, Kirchoff's thermodynamic approach has other implication as such, an object that stay in equilibrium in temperatures above the absolute temperature (0 Kelvin (K) or -273.15 Celsius (℃)) should emit thermal radiation. The spectral radiance of the black body for wavelength (λ) and temperature (T) is explained initially by the Rayleigh-Jeans law using classical arguments:

$$B_\lambda(\lambda, T) = \frac{2ck_BT}{\lambda^4}, \tag{1.5}$$

where c is the speed of light, k_B is the Boltzmann constant, and $B_\lambda(\lambda, T)$ is spectral radiance. There is an issue with this equation known as 'Ultraviolet Catastrophe,' where the spectrum diverges to infinity at the ultraviolet regime [7].

Later, this equation is modified by the Max Planck, assuming that electromagnetic radiation can be emitted or absorbed only in discrete packets called 'quanta,' stating that $E_{quanta} = h\upsilon = h\frac{c}{\lambda}$ where h is Planck's constant. This problem was solved by Albert Einstein and Satyenda Nath Bose, postulating that Max Planck's quanta is a fundamental particle that we call 'photons' [8]. As a result, Max Planck's initial assumption was verified. The modified spectral radiance derived as:

$$B_\lambda(\lambda, T) = \frac{2hc}{\lambda^5}\frac{1}{e^{hc/(\lambda k_B T)-1}}\ , \tag{1.6}$$

and spectral exitance by:

$$M_\lambda(\lambda, T) = \frac{2\pi hc^2}{\lambda^5\left(e^{\frac{hc}{\lambda k_B T}}\right)}, \tag{1.7}$$

$M_\lambda(\lambda, T)$ is the spectral exitance, and its unit is typically derived in the form of power radiated per unit area and wavelength, which is Watt/cm^2-μm. By sweeping the

temperature and wavelength parameters, one can observe the exitance of objects with various temperatures.

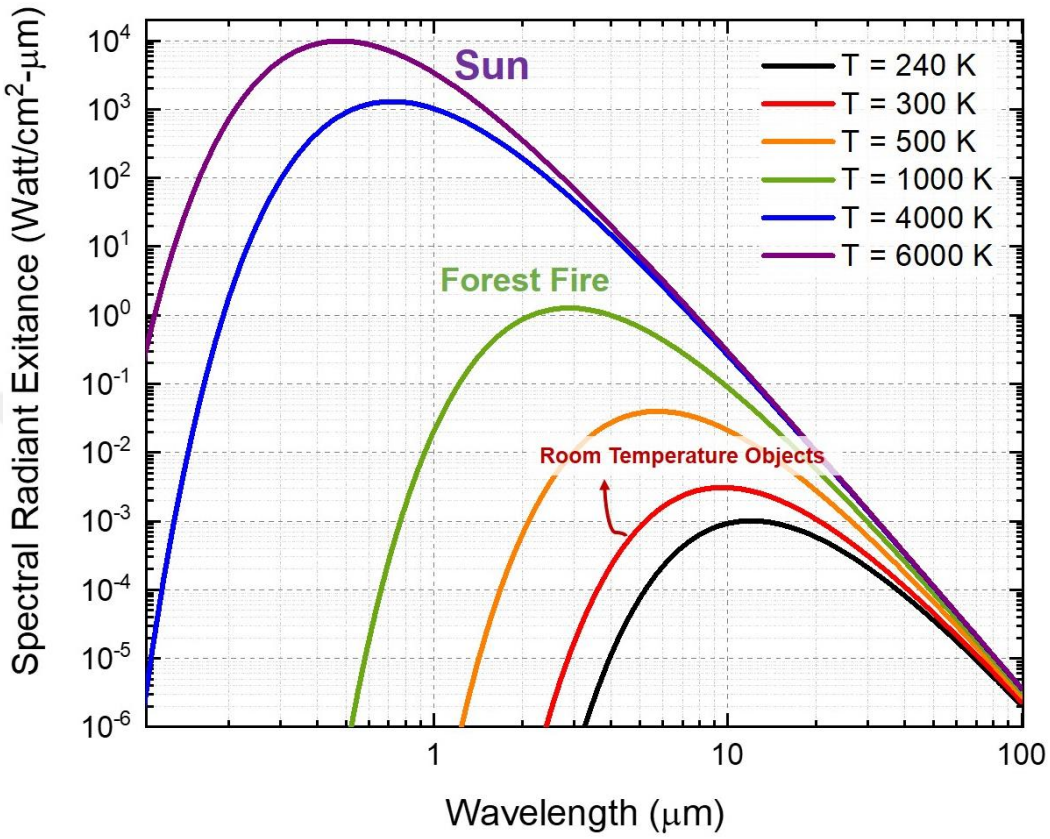


Figure 1.1. Theoretically expected spectral radiant exitance of black bodies with various temperatures vs. wavelength. The given plot is formed by sweeping the wavelength and the designated temperatures in equation 1.7.

From Figure 1.1, one can see that the peak exitance of room temperature objects is around 10 μm wavelength. Also, one can notice that around the 2.5 μm wavelength, exitance power drops to deficient levels. If one wants to detect the photons incoming from the room temperature objects, these points are helpful for which wavelengths to look. Additionally, the exitance spectrum of the Sun peaks between the 400-700 nm wavelength, which coincides with the visible spectrum range. The peak exitance shifts to shorter wavelengths as the temperature of an object gets higher. The peak

exitance wavelength can be estimated by partially differentiating equation 1.7 with respect to wavelength. It is called Wien's displacement law given as follows:

$$\frac{\partial M_\lambda(\lambda,T)}{\partial \lambda} = 0 \quad \rightarrow \quad \lambda_{max} = \frac{2898}{T(K)}\ (\mu m). \tag{1.8}$$

Additionally, one can argue that radiation intensity over all wavelengths proportionally increases with increasing temperature. This phenomenon is explained by the Stefan-Boltzmann law as follows:

$$M_{measured} = \sigma T_{rad}^4 = \varepsilon \sigma T_{true}^4 \quad \rightarrow \quad T_{true} = \frac{T_{rad}}{\sqrt[4]{\varepsilon}}, \tag{1.9}$$

σ is Stefan-Boltzmann constant, ε is the emissivity of the non-ideal blackbody. Once the emissivity is known, the object's temperature can be calculated with the measured exitance.

Exitance contrast is another subject to review as it can be vital for specific applications such as terrestrial imaging. One can find the peak-contrast of the desired object by using the second-order partial derivative of the spectral radiance exitance given by equation 1.7

$$\frac{\partial}{\partial \lambda}\left(\frac{\partial M_\lambda(\lambda,T)}{\partial T}\right) = 0 \quad \rightarrow \ \lambda_{peak-contrast} = \frac{2410}{T(K)}\ (\mu m), \tag{1.10}$$

For the cases of the target and background with very close temperatures, it becomes hard to distinguish the target from the background. Thus, proper choice of operating wavelength becomes crucial. For instance, an object resting at 300 K has a peak exitance at 9.7 μm, whereas the peak exitance contrast at 8 μm wavelength (derived using equations 1.8 and 1.10).

Choosing the best suitable wavelength (or IR-band) is crucial for a desired infrared imaging application. On the other hand, we still need to consider the attenuation and scattering factors as the atmosphere is a good absorber, especially in some portions of the infrared regime.

Interaction of light and matter is quite complicated most of the time, as with the case of atmosphere-photon interaction. The analysis can get quite intense since the atmosphere contains many different gases and particles in various shapes and sizes.

The scattering phenomenon is relatively well understood as we can inspect it mainly with two different scattering types; Rayleigh Scattering and Mie Scattering. The British Physicist Lord Rayleigh first introduced Rayleigh scattering. It is mainly caused by the elastic collision of the photons (IR radiation for our case) and the much smaller particles in size compared to the photons' wavelengths. Rayleigh scattering is strongly wavelength-dependent as the likelihood of happening correlates with the wavelength's inverse fourth power (λ^{-4}). It means shorter wavelengths are much more affected than longer wavelengths. This phenomenon explains the blue color of the sky, as the shorter wavelengths (blue color in the visible band) scatter much more than the longer wavelengths. Thus, incoming blue light from the Sun scatters all around the atmosphere, forming a sensation as if the blue light originates from the sky.

The other type is the Mie scattering. It is also known as the Lorenz-Mie-Debye solution to Maxwell's equations, named after Gustav Mie. It is most effective when the particle size is comparable with the incoming photons' wavelengths. Different weather conditions and dust particles hanging in the air are the main reasons this scattering occurs. For instance, an infrared imaging system operating at the battleground may want to switch IR-bands (assuming it can) under different weather conditions such as foggy, smoggy, or small debris particles hanging in the air.

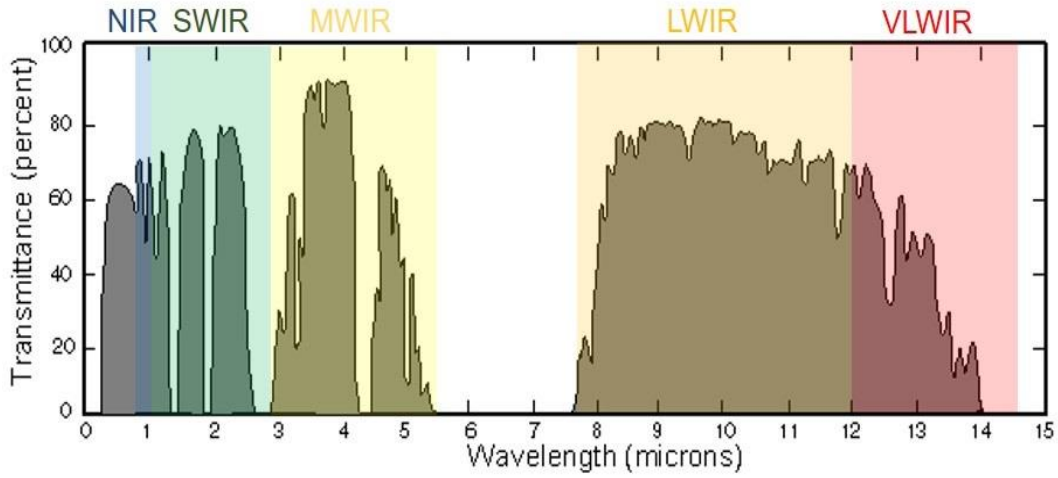


Figure 1.2. The transmittance of the atmosphere for infrared spectrum (redrawn after [9]).

The most noticeable effect for the attenuation of the incoming photons is due to the atmosphere's absorption. As stated before, the absorption analysis is quite intimidating due to the complicated structure of the atmosphere. Molecular bonds and intermolecular interactions are best believed to be the primary reason for infrared absorption. The atmosphere transmittance up to the 15 μm wavelength is given in figure 1.2 [9]. The natural formation of bands can be observed, given atmospheric absorption window between the 5-8 μm wavelength due to the H_2O molecules. Additionally, after 14 μm, CO_2 has another absorption window which precludes infrared imaging in these ranges.

These atmospheric absorption windows constitute the natural formation of the IR bands. The infrared bands given below are also commonly used for classifying the detector technologies:

- Near-Infrared (NIR): 0.7 – 1.0 μm wavelengths
- Short-Wave Infrared (SWIR): 1 – 3 μm wavelengths
    - Extended Short-Wave Infrared (exSWIR or eSWIR) contains the electromagnetic spectrum from 1 μm wavelength to cut-off wavelengths of 1.7 to 3 μm.
- Mid-Wave Infrared (MWIR): 3 – 5 μm wavelengths
- Long-Wave Infrared (LWIR): 8 – 12 μm wavelengths
- Very Long-Wave Infrared (VLWIR): 12 – 20 μm wavelengths
- Far Infrared (FIR): 20 – 1000 μm wavelengths

IR imaging systems built upon an array of pixels are called focal plane arrays (FPA). FPAs require optics to make imaging possible. Optics are one of the integral factors in infrared imaging systems; designing an optical system requires particular expertise. For this work, optical system design is not a concern; however, to know the optical limitations may affect the design and fabrication processes of the IR photodetectors.

The diffraction limit is an essential point while designing an FPA. It is referred to as Rayleigh Criterion, and it estimates the diameter of the airy disks by:

$$\mathrm{D} \approx 2.44 * \lambda * (f/\#), \tag{1.11}$$

D is the diameter of the forming airy ring, $f/\#$ is the f-number of the optics. For instance, for an FPA operating in the LWIR band with a cut-off wavelength of 10 μm, the diameter of the airy disk is 24.4 μm using f/1 optics. In other words, incoming thermal radiation from an object forms a blurry-disk spot with a diameter of 24.4 μm. To extract this information completely, the pixel size (pitch) should be no less than 24.4 μm. The airy disk that falls on FPA stays on more than one pixel for smaller pitch sizes — or saying that the same information is passed on to the neighboring pixels, called cross-talk.

The diffraction limit is most likely to define the minimum pitch sizes of the desired IR imaging systems. Even though 24.4 μm looks like a small number, it brings an issue when fabricating a mega-pixel FPA in terms of operability and performance uniformity.

This thesis offers a new method to decrease the surface leakage current of an infrared detector. An InGaAs/InP SWIR sample with a cut-off wavelength of 1.69 μm is processed to prove this concept. Figure 1.1 indicates that room-temperature objects have little to no radiation emission at the SWIR band. Thus, thermal imaging is not possible for SWIR detectors. Sun and Moon reflecting sunlight at night are the primary sources of infrared radiation. Reflected emission from these sources is essential for imaging in the SWIR band.

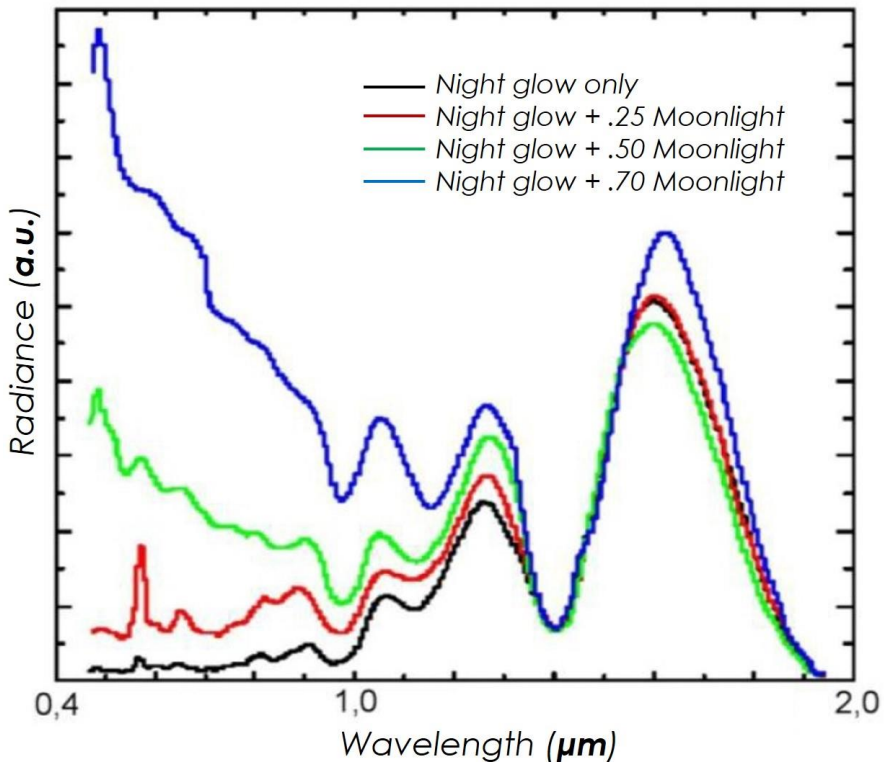


Figure 1.3. Spectral radiance at night due to night glow and different moon conditions (redrawn after [10]).

Night vision in the moonless night is also possible due to a phenomenon called airglow. Airglow is the radiation caused by the relaxation of the hydroxyl (OH)

molecules in the air. OH molecules are excited during the daytime, releasing the photons at night that coincide with the SWIR wavelengths [10]. The radiance spectrum of airglow with different moon conditions is illustrated in figure 1.3.

1.2 Properties and Figures of Merit for Infrared Detectors

Rigorous methods are required to compare the performance of the infrared detectors. This part covers the merits of infrared detectors commonly used by researchers and experts in this field.

1.2.1 Dark Current of a Photovoltaic Detector

The dark current of a p-n junction can be explained with various current mechanisms. It can be divided into two main components: bulk and surface current. Bulk current can be estimated with the sum of diffusion current, generation-recombination current, tunneling current, and shunt current; surface current can be investigated with generation-recombination current, tunneling current, and additional surface leakages [26].

The total dark current can be explained in the following simplified manner:

$$I_{dark} = I_{diff} + I_{g-r} + I_{shunt}\,, \tag{1.12}$$

Diffusion Current is governed by Fick's laws. He initially explained it as the mass transport through diffusive means in fluids, later, it is used to explain the diffusive processes in a semiconductor. Due to thermal carrier generation, carriers flowing from higher concentration to the lower concentration region produce this current type. Diffusion current in terms of applied voltage described by:

$$I_{diff}(V) = I_S\,(e^{qV/k_BT} - 1)\,, \tag{1.13}$$

I_s is denoted as reverse-saturation current. q, k_B, T, are electron charge, Boltzmann constant, and temperature, respectively. Assuming a long diode condition where the length of the n and p doped layers are longer than the diffusion lengths, I_s yields to:

$$I_S = qA\left(\frac{L_p}{\tau_p}\frac{n_i^2}{N_D} + \frac{L_n}{\tau_n}\frac{n_i^2}{N_A}\right), \tag{1.14}$$

where τ_p, τ_n are minority carrier lifetimes, n_i^2/N_D, n_i^2/N_A are minority carrier concentrations calculated by dividing the square of intrinsic concentration by acceptor/donor doping densities. L_p, L_n are minority carrier diffusion lengths which equal to:

$$L_{n,p} = \sqrt{D_{n,p}\,\tau_{n,p}}, \tag{1.15}$$

where $\tau_{n,p}$ is carrier recombination lifetime, and $D_{n,p}$ is diffusion coefficient which is explained by Einstein coefficient in terms of mobility, Boltzmann constant, electron charge, and temperature:

$$D_{n,p} = \mu_{n,p}\frac{k_B T}{q}. \tag{1.16}$$

Generation-Recombination (GR) current flows mainly due to trap centers inside the forbidden gap of a semiconductor. Shockley-Read-Hall (SRH) explains it, denoted as SRH recombination. These trap centers are most effective when their energy state is at the mid-band and occurs in the depletion region. Point defects are the main reason why GR processes occur [27]. The SRH recombination process is explained in equation 3.1-2. Additionally, other recombination processes such as radiative and Auger contribute to the GR current. The effective GR lifetime can be explained as:

$$\frac{1}{\tau_{eff}} = \frac{1}{\tau_{radiative}} + \frac{1}{\tau_{Auger}} + \frac{1}{\tau_{SRH}} + \frac{2S}{d}, \tag{1.17}$$

$\tau_{radiative}$, τ_{auger}, τ_{SRH} are radiative lifetime, effective Auger lifetime, and effective SRH lifetime respectively, S is the surface recombination velocity and d is thickness

of active surface layer. Further stating that GR processes are the most effective at the depletion layer; GR current is estimated by:

$$I_{gr} = \frac{qA\, n_i W_{dep}}{\tau_{eff}} \left(e^{\frac{qV}{2k_B T}} - 1 \right), \tag{1.18}$$

τ_{eff} is effective GR lifetime. Depletion layer width W_{dep} is expressed as:

$$W_{dep} = \sqrt{\frac{2\varepsilon}{q} \left(\frac{1}{N_A} + \frac{1}{N_D} \right) (V_{bi} - V)}, \tag{1.19}$$

ε is the permittivity of the semiconductor and V_{bi} is expressed as:

$$V_{bi} = \frac{k_B T}{q} \ln \left(\frac{N_A N_D}{n_i^2} \right) \tag{1.20}$$

Ohmic Leakage or Shunt Current is caused by manufacturing defects. Namely, the line defects (dislocations) and the surface defects such as grain boundaries constitute this type of mechanism [27]. Therefore, both surface and growth conditions are effective in forming shunt resistance/current, given as:

$$I_{shunt} = \frac{V}{R_{shunt}} \tag{1.21}$$

1.2.2 Quantum Efficiency and Responsivity

Quantum efficiency is a measure of generated electron-hole pairs per incident photon. The detector-photon interaction can be explained by Kirchoff's law, defined with equations 1.1, 1.2.

Initially, there exist incident photons. Some of the incident power is reflected at the interface of the detector. Some radiation power is absorbed, results in current flowing, and the rest is transmitted through the detector. Reflections from the surface of the detector can be decreased by depositing an anti-reflecting coating (ARC) to the surface. Absorption can be increased by increasing the active layer's thickness,

thus decreasing the transmission. These factors can be optimized by considering the other device parameters, such as diffusion length, resulting in higher quantum efficiency and higher responsivity. Quantum efficiency can be given as:

$$\eta_Q = \frac{collected\ electron\ hole\ pairs}{photons\ reaching\ to\ active\ layer'}, \tag{1.22}$$

$$\eta_X = \frac{collected\ electron\ hole\ pairs}{incident\ photons} = \frac{\eta_Q\ (1-r)(1-e^{-\alpha t})}{1-re^{-\alpha t}}, \tag{1.23}$$

η_Q is internal quantum efficiency, whereas η_X is external quantum efficiency and is directly related to the responsivity of the detector. r, α, t parameters are the reflection coefficient, absorption coefficient, and the active layer thickness of the detector, respectively. The relation between the quantum efficiency and the responsivity of a photovoltaic detector can be given as:

$$\eta_X = \frac{collected\ electron-hole\ pairs}{incident\ photons} = \frac{I_L/q}{P_{in}/E_{photon}} = \frac{hc}{\lambda q}R, \tag{1.24}$$

I_L is the current flowing at the load, P_{in} is incident photon power, and R being the responsivity. Responsivity determines the magnitude of response of the detector for an incident photon flux. Rearranging equation 1.14:

$$R = \frac{output\ signal}{input\ power} = \frac{I_L}{P_{in}} = \lambda g\eta\frac{q}{hc} = \frac{\lambda(\mu m)}{1.24}g\eta \quad (A/W), \tag{1.25}$$

an additional g parameter called gain is caused by the internal gain mechanisms of some detector types, such as photoconductive detectors.

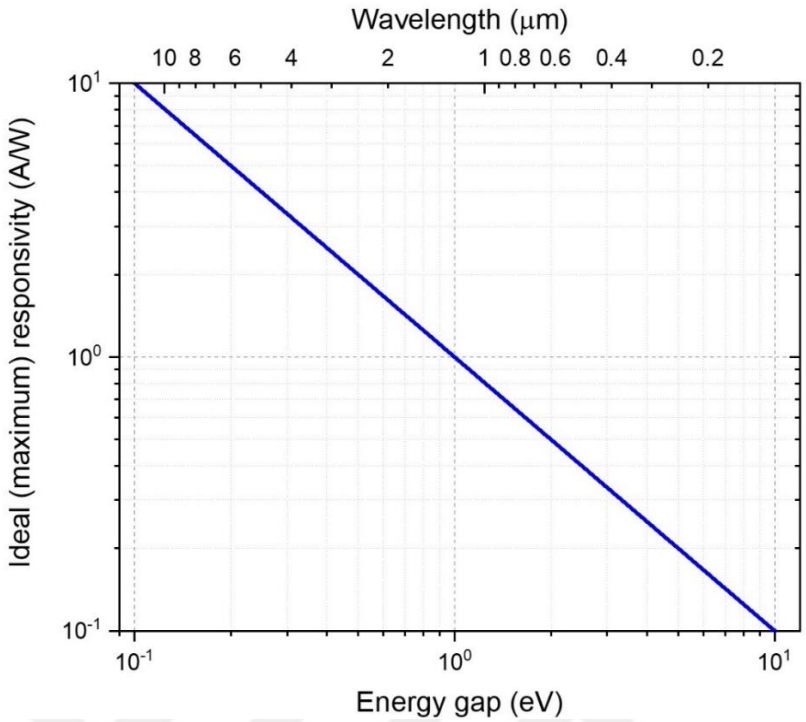


Figure 1.4. Ideal responsivity versus energy gap and wavelength (redrawn after [11]).

The ideal responsivity that a detector can reach is given in figure 1.4. One can notice that it is inversely proportional to the wavelength, as inferred from equation 1.25. A blackbody source is commonly used for the responsivity measurements since it is much cheaper and widely available than its tunable narrowband counterparts. In that case:

$$R_{BB}(T) = \frac{output\ signal}{blackbody\ power} = \frac{\int_0^\infty R(\lambda)\phi(\lambda)d\lambda}{\int_0^\infty \phi(\lambda)d\lambda}. \tag{1.26}$$

Blackbody responsivity is defined as the produced response of a detector with an input optical radiation of 1 Watt of power.

The responsivity alone is insufficient merit to define the ultimate performance of the detector. The detector may have high noise levels, resulting in an inadequate signal-to-noise ratio (SNR or S/N).

1.2.3 Various Noise Mechanisms

Noise is described as unwanted oscillations at the output signal. Various sources and mechanisms acting upon the detector cause these signal variations; thus, they should be reviewed in their context.

1.2.3.1 Johnson-Nyquist (Thermal) Noise

Thermal fluctuations or thermal agitation of the carrier charges (electron or holes in a semiconductor) inside a conductor causes this type of noise. It is temperature dependant. As long as an absorption process exists, this type of noise should never decay entirely according to the fluctuation-dissipation theorem, even at the absolute zero temperature. It is known to be almost wholly frequency independent (white), except for extremely high frequencies and near absolute zero temperatures due to the quantum effects [12].

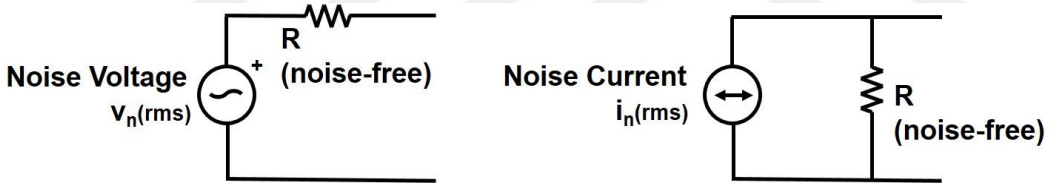


Figure 1.5. Equivalent circuits for Johnson-Nyquist noise.

Circuit representation for the thermal noise is given in figure 1.5. Noise current spectral density and noise voltage spectral density is calculated with:

$$V_n(rms) = \sqrt{4k_BTR}\,\left(V/\sqrt{Hz}\right)\ or\ \ I_n(rms) = \sqrt{\frac{4k_BT}{R}}\ (A/\sqrt{Hz}), \qquad (1.27)$$

R is the dynamic resistance of the detector. Noise voltage or current defined as:

$$V_n(rms) = \sqrt{4k_BTR\Delta f}\ (Volts)\ or\ \ I_n(rms) = \sqrt{\frac{4k_BT\Delta f}{R}}\ (Amps), \qquad (1.28)$$

where Δf is the measurement bandwidth.

1.2.3.2 Shot (Poisson) Noise

Shot noise is a prominent noise mechanism in IR-detector technology. It occurs due to the discrete nature of the photons and electric charge. Hence, both the dark current and the photocurrent acting upon the detector contribute to this type of noise. For the photovoltaic detectors operating at the MWIR and LWIR bands, shot noise is dominant in most cases because the exitance of the room temperature objects is high enough. On the other hand, it may not be the case for the devices operating at SWIR band depending on the operation conditions, i.e., daytime or nighttime imaging.

The nature of the shot noise can be explained similarly to a coin toss experiment. As the number of coin tosses increases, fluctuations will decay, and the result of the actual experiment will converge to the expected value of the experiment. Similarly, for the photon counting devices (such as photon detectors), as the integrated number of photons increases, fluctuations decay, noise is said to be decreased. As the law of large numbers suggests, relative fluctuations are going to decay with the mean square of the root of the photon or carrier number. The average number of carriers is defined as:

$$\overline{N} = \frac{I}{q}\Delta t \tag{1.29}$$

The variance of the number of carriers can be defined statistically; recall random variable statistics for a Poisson distribution:

$$rms\ variance\ (noise) = \sqrt{\overline{\left(N - \overline{N}\right)^2}} = \sqrt{\overline{N}}, \tag{1.30}$$

thus shot noise can be determined by:

$$\frac{S}{N} = \frac{\overline{N}}{\sqrt{\overline{N}}} = \sqrt{\overline{N}} \ \rightarrow \ \overline{i_n} = q\frac{\sqrt{\overline{N}}}{\Delta t} = \sqrt{2qI_{tot}\Delta f}\ \ (Amps), \tag{1.31}$$

q is electric charge, I_{tot} is the sum of photo and dark currents, and Δf is the measurement bandwidth. Dividing equation 1.31 with $\sqrt{\Delta f}$ results in spectral noise density that is frequency independent; thus, shot noise is said to be white noise.

1.2.3.3 1/f (Pink) Noise

This phenomenon is observed in semiconductors and the various fields and concepts such as in biophysics, different magnitude earthquakes, and diffusion processes [13]. Empirical methods are used for expressing this type of noise since the exact origin of the 1/f noise is still unknown. It is dominant at lower frequencies and becomes relatively negligible at higher frequencies. A representative graph of noise current with respect to frequency is given in figure 1.6.

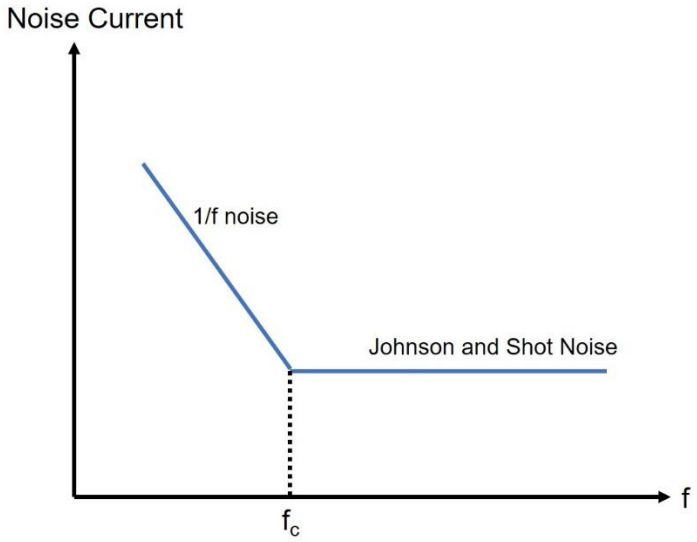


Figure 1.6. A typical frequency spectrum of a noise current with respect to measured frequency.

Other types of noise mechanisms exist, such as capacitor noise and generation recombination noise which are typically not dominant. The total noise current can be calculated with the mean-rms currents of the noise processes:

$$i^2_{total-noise} = i^2_{Johnson} + i^2_{shot} + i^2_{1/f} + i^2_{other-sources} \tag{1.32}$$

The typical noise sources in a photovoltaic (PV) detector are:

- **Shot noise** caused by both the dark current and photocurrent. Photocurrent noise can be explained as the feedback noise of the signal and the background.
- **Johnson noise** occurs due to detector resistance and load resistance. Combination of detector resistance and the read-out integrated circuit (ROIC) input resistance.
- **1/f noise** caused by the current flow.
- Noise associated with the preamplifier circuit and preamplifier output noise voltage.

1.3 Noise Equivalent Power and Specific Detectivity

Noise equivalent power (NEP) is an expression for required radiant flux to generate an output signal equal to the detector's noise. In other words, radiant power incident on the detector to have an SNR of 1. The NEP expression in terms of responsivity and rms noise:

$$NEP = \frac{v_{noise,rms}}{R_v} = \frac{i_{noise_rms}}{R_i} = \frac{\phi_{signal}}{SNR} \quad (Watts). \qquad (1.33)$$

Smaller NEP means higher detector sensitivity. NEP itself is not a sufficient figure of merit to describe the detector performance because it is dependent on detector area and electronic bandwidth.

The detectivity (D) of a detector is expressed with 1/NEP. Since the NEP depends on the detector area and bandwidth, the detectivity (1/NEP) is also a poor figure of merit in comparing different detector mechanisms or materials. By normalizing the detectivity with noise-equivalent bandwidth and detector area, we get normalized detectivity. The normalized or specific detectivity (D^*) is often used as a good

predictor of the performance of an infrared detector. The specific detectivity expression is directly proportional with the SNR and the responsivity, defined as:

$$D^* = \frac{\sqrt{A_d \Delta f}}{NEP} = \frac{\sqrt{A_d \Delta f}}{\phi_d} SNR = \frac{\sqrt{A_d \Delta f}}{i_n} R_i, \qquad \left(\frac{cm\sqrt{Hz}}{Watt}\right) \tag{1.34}$$

$$or \quad D^* = \frac{\sqrt{A_d \Delta f}}{v_n} R_v, \qquad \left(\frac{cm\sqrt{Hz}}{Watt}\right) \tag{1.35}$$

The plot of a spectral-specific detectivity $D^*(\lambda)$ of a photon detector is given in figure 1.7. The spectral specific detectivity can be determined as follows:

$$D^*(\lambda) = D^*_{peak}(\lambda_{cut-off}) \frac{\lambda}{\lambda_{cut-off}}. \tag{1.36}$$

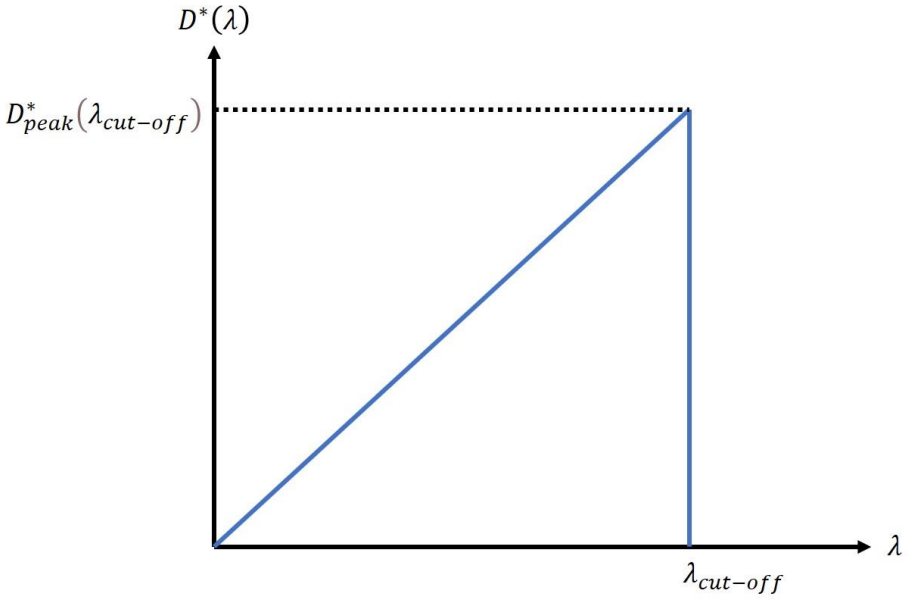


Figure 1.7. Spectral specific detectivity of a photon detector.

1.4 Noise Equivalent Temperature Difference

Noise equivalent temperature difference (NETD) is the minimum detectable temperature difference of an object with respect to the background radiation. Thus,

lower NETD means higher detector performance. The NETD expression is determined as follows:

$$NETD = \frac{[4(f/\#)^2 + 1]\sqrt{\Delta f}}{\sqrt{\mathrm{A}_d}\int_0^\infty T(\lambda)\, D^*(\lambda)\frac{dM_{target}(D^*(\lambda))}{dT}\, d\lambda} \tag{1.37}$$

f/# is the f-number of the used optics, *D** is the specific detectivity, *T* is atmospheric transmission, and *M* is the spectral exitance of the target object. The biggest drawback of the NETD is its dependency on *f/#* of the used optics. Smaller f/# optics requires bulkier optics, resulting in lower NETD. Thus, the used optics should be identified to compare NETD values of the different photodetectors.

1.5 Noise Equivalent Irradiance

Noise equivalent irradiance (NEI) is the flux density at the entrance of optics to generate an output signal-to-noise ratio (SNR) of 1. Noise equivalent irradiance, also referred to as noise equivalent flux density (NEFD), is defined in terms of f-number:

$$NEI_{BLIP} = \frac{2hc}{\lambda_{cut-off} D_{opt} \tau_{opt} \tau_{atm}} \frac{\sqrt{2\Omega_\mathrm{d}\Delta f \int_0^{\lambda_{cut-off}} L_{p,bkg} d\lambda}}{\pi\eta} \tag{1.38}$$

Ω_d is detector solid angle, D_{opt} is the diameter of the optics and τ_{opt}, τ_{atm} are optical transmittance and atmospheric transmittance between the point source and the detector system, $L_{p,bkg}$ is background radiance and η is the factor (typically 2) related to switching between measuring a source and off-source. NEI can be interpreted as an average over a spectral interval or as the peak value. It is used to characterize the entire system's performance; however, it can also be defined as radiant flux density to produce an SNR of 1. In that case, it can be used to determine the performance of the different area detectors [25]:

$$NEI = \frac{E}{SNR} = \frac{NEP}{A_d} \tag{1.39}$$

E is irradiance and A_d is the area of the detector.

CHAPTER 2

BRIEF SUMMARY OF PHOTOVOLTAIC SWIR TECHNOLOGIES

Photovoltaic SWIR detector technologies are covered in this chapter. Application areas for SWIR photodetectors are introduced, and properties used in a given field are discussed. Types of SWIR photodetectors with different material systems are reviewed for desired applications.

2.1 Various Applications for SWIR Photodetectors

SWIR photodetector technologies are employed for medical imaging, optical communication, deep space exploration, quality control for commercial products, and commonly for military applications.

Human bones are transparent at the SWIR band. Thus, by using an illumination source, one can observe the veins and arteries of a human body. A NIR/SWIR InGaAs camera reflects the details of the veins of an arm [14]. It may be used in the early diagnosis of vascular diseases; also, surgical complications may be avoided with these medical images.

Deep space observation is one of the application areas of a SWIR detector. Very recently, the most powerful manmade telescope was launched to the second Lagrange (L2) Earth orbit, which is approximately 1.5 million kilometers away from Earth. Named after James Webb, James Webb Space Telescope equipped with various infrared detectors has a mission to observe deep space high-redshift distant objects. These distant stellar objects might be holding the secrets of how the universe is formed, and this mission is expected to give us clues about them.

This controversial project cost a whopping 10 billion USD since its inception in 1997. Many risks involved with this engineering marvel caused its launch to be postponed many times over the years. The mission duration is planned to be 10 years after starting the duty. When it becomes online, it is going to be the most powerful telescope with infrared detectors standing at the heart of it. It has a total of 18 infrared detectors with various cut-off wavelengths. The Near Infrared Camera (NIRCam) of the James Webb Space Telescope can detect photons with wavelengths 0.6 – 2.5 μm long, covering NIR and SWIR and extended-SWIR bands. This mercury-cadmium-telluride (MCT) detector (with product line name of H2RG) was made by Teledyne Imaging Sensors in California, US [15].

Thermal radiation of room temperature objects at the SWIR band is fairly low compared to the MWIR and LWIR bands observed in figure 1.1. Typically, thermally generated photocurrent is comparable to the noise of the detector-ROIC couple in the SWIR band. Thus, MWIR and LWIR bands offer much better results for thermal imaging.

Although the exitance of the room temperature objects at the SWIR band is quite low, photons originating from the Sun enable SWIR imaging. Similar to the operation of visible imaging using a CMOS camera, it is possible to form an image with the reflected infrared radiation from the objects.

Regardless the origin of the photons, the SWIR band has advantages over the visible band due to the transmission of the atmosphere and objects. Where the ambient conditions such as haze and fog exist, it is possible to observe objects using a SWIR photodetector, whereas the visible band is not useful. Scattering through cloud, haze, smoke, and fog of SWIR radiation is explained in Driggers et al. [28]. Additionally, lasers with 1550 nm and 850 nm wavelengths are used for target designation for tactical missile systems. In that case, SWIR imaging sensors are useful for finding and locking to the target accurately [17].

For military applications, generally, many detectors and sensors in different electromagnetic bands such as SWIR, MWIR, LWIR, visible cameras, and radar

systems are used together to complement each other. The information provided by these systems vitally dictates the warfare conditions; hence, military personnel is heavily dependent on these.

Similarly, for the deep space explorations, more information resolves to better understanding. Thus, space applications utilize various spectral bands to observe, and they are limited by the performance of the corresponding detector systems.

2.2 Common SWIR Photovoltaic Detectors

To understand the SWIR photodetectors, they should be analyzed with the area of interest of the given system. For some applications, absolute performance is the key interest for such military equipment, and for some others, different environment and operation conditions may determine its usefulness. For instance, Germanium (Ge) can be used as a SWIR photodetector in an optical communication system because it can be utilized in an integrated circuit monolithically. Moreover, extrinsic factors, including the cost of the detector system and the desired operation conditions, mandate certain tradeoffs. Considering all these factors, research in this field converged to certain materials and photodetector systems.

Germanium (Ge) is a semiconductor with unique features. In its natural crystal formation, it is an indirect bandgap material; however, various techniques such as inducing strain or alloying with Tin (Sn) allow it a transition to direct bandgap illustrated in figure 2.1 [18]. Employing these manipulations, Ge grown on Si offers infrared imaging up to 1.6 μm wavelength [19].

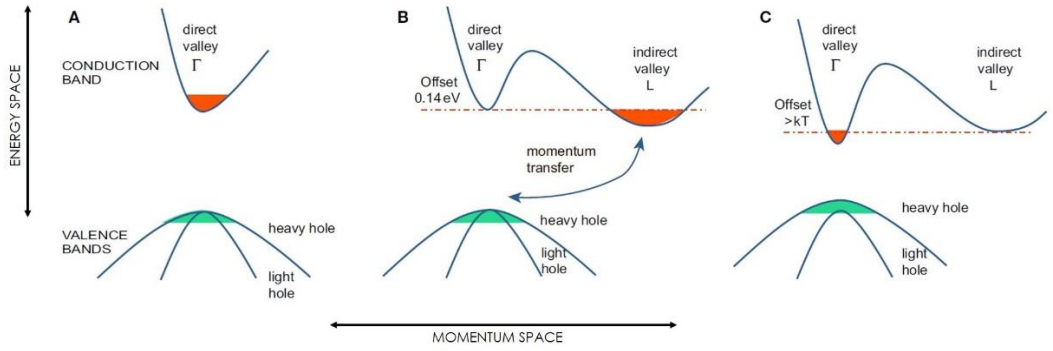


Figure 2.1. Band structure in energy-momentum space. **(A)** Typical direct bandgap semiconductor. **(B)** Band diagram of Ge, electrons occupy the indirect L-valley. **(C)** Inducing strain to Ge or alloying with Sn decreases the bandgap, resulting in a population increase in Γ-valley (redrawn after [19]).

SWIR Ge photodetector with a 10 μm pitch length has been reported to have an average dark current of 28 fA at -45 ℃ temperature. Reported quantum efficiency (QE) is 34% at 1.3 μm [19].

Ge offers a low-cost solution, and results are promising; yet, research in Ge photodetectors for SWIR imaging is relatively uncommon because of its low quantum efficiency, shorter peak responsivity wavelength, and indirect bandgap. Under these conditions, Ge is perhaps more suitable for communication purposes in photonic integrated circuits due to its low cost and ability to monolithic integration to CMOS processes rather than SWIR imaging.

Mercury-Cadmium-Telluride ($Hg_{1-x}Cd_xTe$) (MCT) is a natural infrared photodetector material. HgCdTe is a ternary alloy with perfect properties tailored for all infrared spectrum. MCT photodetector technology offers huge control over its bandgap; thus, by changing the mole fractions of Mercury (Hg) and Cadmium (Cd), it is possible to fabricate photodetectors in SWIR (starting ~1 μm) to VLWIR bands (up to 30 μm). Additionally, it is a direct bandgap material with high absorption coefficient, and its lattice constant does not change much for changing the mole fraction of x. These unique properties of MCT put it in a very critical position [29].

The bandgap and the lattice constant variation of MCT with respect to mole fraction are plotted in figure 2.2.

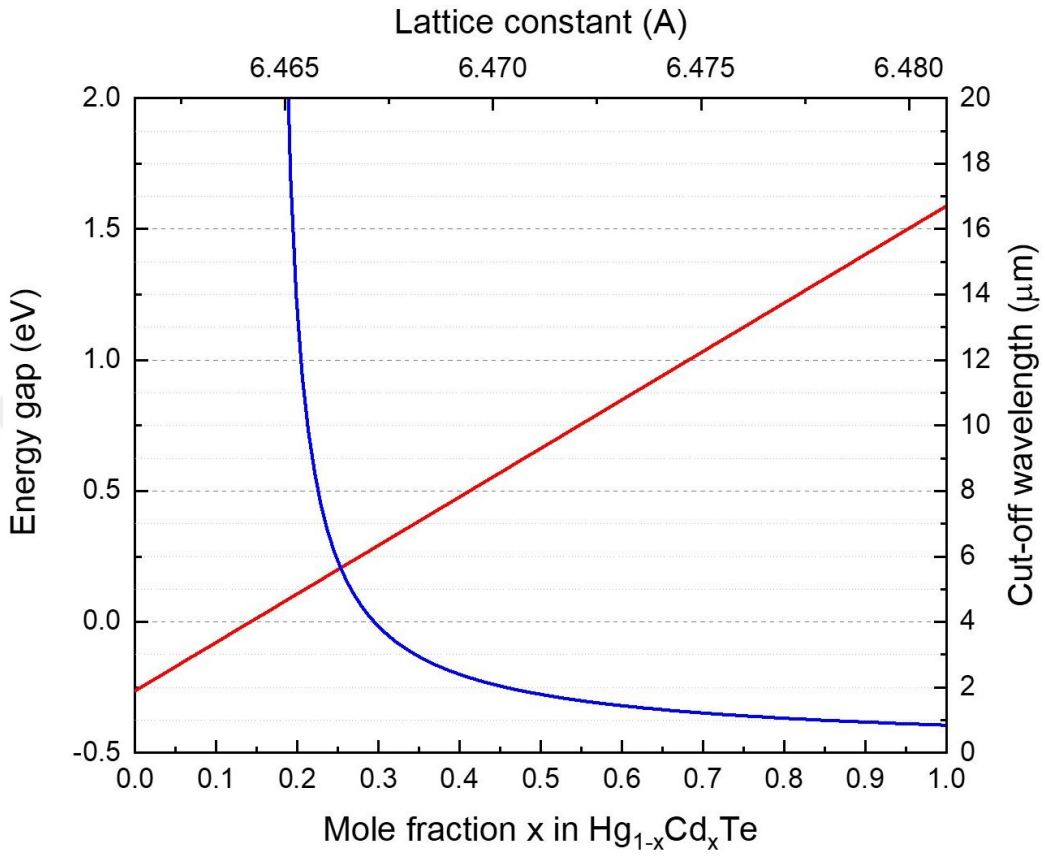


Figure 2.2. Energy gap and the cut-off wavelength of $Hg_{1-x}Cd_xTe$ with corresponding lattice constant and mole fraction (x) at 77 K.

Typically, high-performance MCT photodetectors are grown on lattice-matched Cadmium-Zinc-Telluride (CZT) substrate. It is also possible to fabricate MCT photodetectors on alternative substrates such as Silicon, but it comes with a compromise in the detector's performance [30]. One of the major drawbacks of the MCT is the cost and the availability of high-quality CZT substrates. The other factors include non-uniformities for large-scale applications, high-cost less-yield growth and processing, and bad surface stability. These conditions make MCT a challenging material; yet, its perfect properties render it indispensable, especially for LWIR applications.

The biggest advantage of MCT in SWIR applications is its finely-tunable bandgap compared to mature InGaAs/InP photodetectors. The biggest limitation of the SWIR band is the low photon exitance of the room temperature objects in this regime. The extended SWIR photodetectors offer higher image quality due to photon exitance and higher contrast because of the different emissivity of the objects. Finely-tuned lattice-matched MCT photodetectors offer a dark current density of 2 nA/cm^{-2} at 240 K temperature with extended-SWIR cut-off wavelength of 2.5 μm [31]. Compared to InGaAs SWIR photodetectors, $In_{1-x}Ga_xAs$ is only lattice-matched to InP substrates when mole fraction x=0.47, providing a shorter cut-off wavelength of 1.7 μm. Thus, extended SWIR wavelengths are the best place for MCT photodetectors in SWIR technology.

Indium-Gallium-Arsenide ($In_{1-x}Ga_xAs$) is the key material for SWIR imaging. InGaAs grown on InP photodetectors is one of the most mature technology in infrared imaging. InGaAs' great properties combined with the availability and lower cost of high-quality InP substrates bring InGaAs SWIR photodetectors versatility in the SWIR market. InGaAs' intrinsic qualities include high quantum efficiency, high electron mobility, and high absorption coefficient [32]. The mature fabrication technology led to good quality lattice-matched InGaAs/InP photodetectors operating near room temperatures.

Selected $In_{0.53}Ga_{0.47}As$ and InP parameters at 300 K is given in table 2.1 and 2.2, respectively. These parameters are also used in calculations in the next chapter.

Table 2.1 $In_{0.53}Ga_{0.47}As$ Material Parameters at 300 K

Parameter	*Value*	*Reference*
Bandgap	0.74 eV	[33]
Lattice constant	5.8687 A	[34]
Intrinsic carrier concentration (n_i)	6.3×10^{11} cm^{-3}	[35]
Static relative permittivity (ϵ_r)	13.1 – 14.1	[36]
Bulk electron mobility ($\mu_{n,bulk}$)	$> 10^4$ $cm^2/V{\cdot}s$	[37]
Surface electron mobility ($\mu_{n,surface}$)	1500 – 2600 $cm^2/V{\cdot}s$	[38]
Surface carrier density (2DEG) (n_s)	2.3×10^{12} cm^{-2} 3.1×10^{12} cm^{-2}	[38]

Table 2.2 InP Material Parameters at 300 K

Parameter	*Value*	*Reference*
Bandgap	0.74 eV	[39]
Lattice constant	5.8687 A	[40]
Intrinsic carrier concentration (n_i)	1.3 x 10^7 cm^{-3}	[41]
Static relative permittivity (ϵ_r)	12.5	[41]

Mesa type and planar type InGaAs/InP photodetectors are employed in this field. The structure and fabrication of mesa-type photodetectors are explained in chapter 3. The planar type InGaAs/InP structure is given in figure 2.3 and mesa type in figure 2.4.

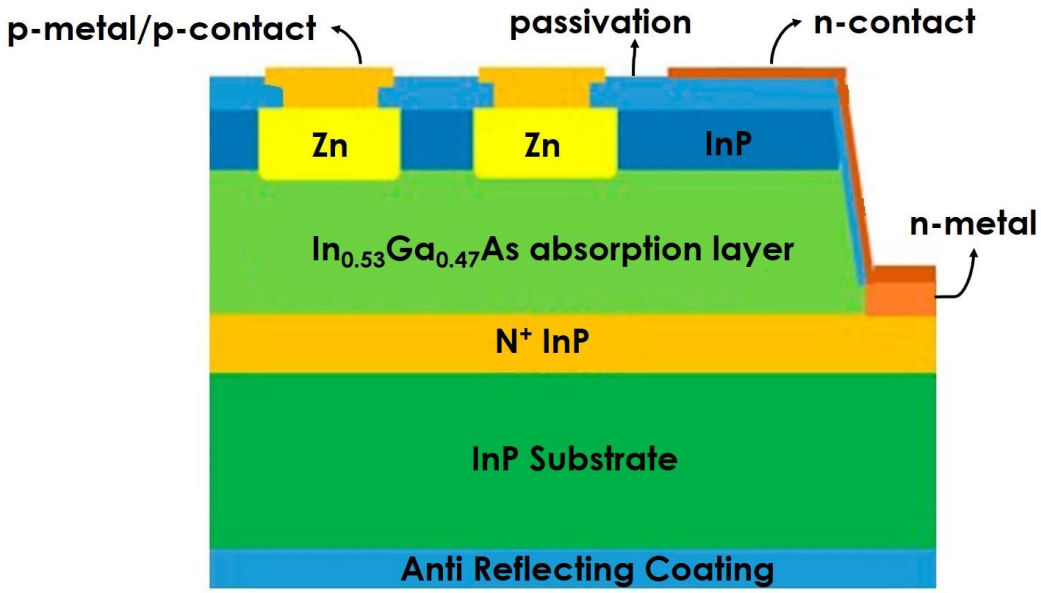


Figure 2.3. Typical SWIR planar InGaAs/InP structure (redrawn after [42]).

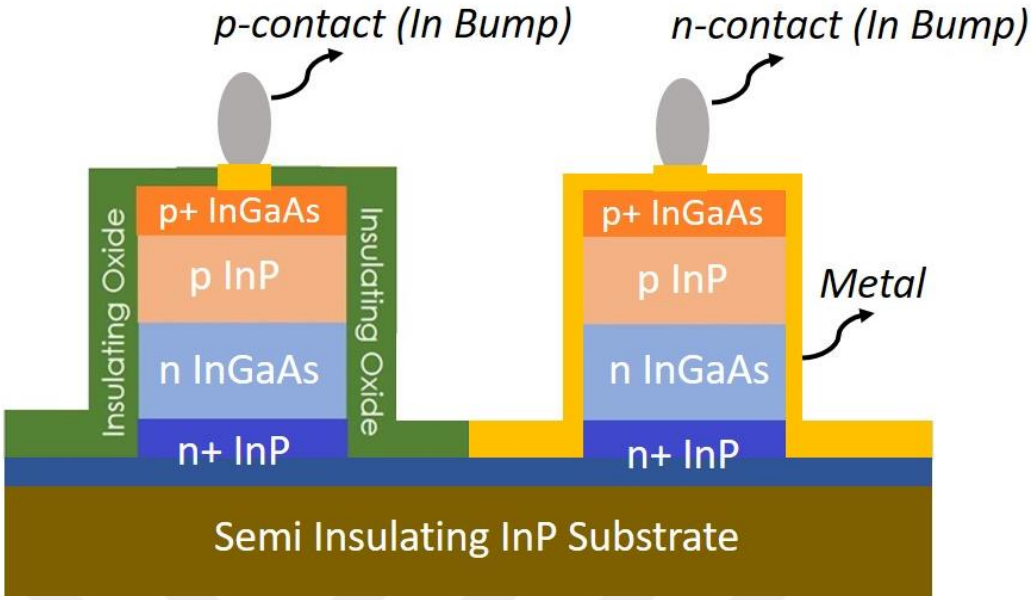


Figure 2.4. Mesa type SWIR InGaAs/InP structure.

Planar type photodetectors offer much better performance than mesa type in terms of dark current density and specific detectivity. The state-of-the-art performance in SWIR is listed in table 2.3. The dark current density of 2.3 nA/cm^{-2} and specific detectivity higher than 10^{13} cm·Hz$^{1/2}$W^{-1} are reported at room temperature [42].

The biggest drawback of mesa structure–the surface leakage is mostly overcome in planar type. On the other hand, the pixel isolation in mesa structure does not exist in planar type. Thus, planar-type SWIR photodetectors are prone to cross-talk. Moreover, it impossible to produce a dual-band/dual-color planar photodetector. Therefore, mesa-type photodetectors are still being used even though their performance does not match the planar types.

Table 2.3 State-of-the-art performance comparison of planar type InGaAs/InP SWIR photodetectors.

Reference	*Dark Current* *(nA/cm^{-2})*	*D** *($cm\cdot Hz^{1/2}W^{-1}$)*	*QE* *(%)*	*Operability*
Zhang et al. [42]	2.3 @ RT	$1.1x10^{13}$	88%	> 99.9%
Li et al. [43]	< 5 @ RT	$5\ x10^{12}$	75%	> 99%
Fraenkel et al. [44]	0.5 @ 280 K	$> 10^{13}$	80%	> 99.5%
Macdougal et al. [45]	3.8 @ RT	$> 10^{13}$	80%	99.98%
Hood et al. [46]	< 1 @ 285 K	$> 10^{13}$	70%	> 99.5%
Dixon et al. [47]	2 @ 282.5 K	$> 10^{13}$	65%	> 99%
Yuan et al. [48]	0.7 @ 280 K	$> 10^{13}$	80%	> 99%

CHAPTER 3

FABRICATION AND CHARACTERIZATION OF InGaAs/InP SWIR INFRARED TEST DETECTOR WITH ACTIVE SURFACE PASSIVATION

A novel method for surface passivation of InGaAs/InP photodetectors is introduced in this chapter. As a proof of concept, a molecular beam epitaxy (MBE) grown InGaAs/InP on InP substrate is fabricated, and device performance is evaluated. Fabrication steps for this technique are explained, and the characterization methods and results are submitted accordingly.

3.1 A Discussion Regarding the Surface Recombination and Fixed Charges

The surface phenomenon is first described by Tamm (1932), stating that the existence of a crystal surface cuts off the periodic potential field of the semiconductor. It yields the surface to generate additional energy levels that stand in the forbidden gap of the semiconductor [21]. This analysis is hard enough for more than a single trap energy level; it is much more complicated for the actual surfaces due to the oxidization and impurities of the crystal surface. Hence, a one-dimensional crystal surface under the ideal conditions is discussed in formulization.

Surface recombination is a non-equilibrium carrier recombination process, and the surface recombination rate is explained as an extension of the Shockley-Read-Hall (SRH) theory. Suppose a surface contains uniformly distributed recombination centers with a density of N_T, and all of these centers are located at the $E_i - e\phi_s$. The recombination rate of these centers is defined with its capture cross-sections and electron and hole densities at the surface. Assuming a nondegenerate electron and hole distribution, using statistical analysis to get recombination rate per unit area:

$$r_s = \frac{N_T c_p c_n (p_b + n_b)\Delta p}{c_p(p_s + p_{s1}) + c_n(n_s + n_{s1})}, \tag{3.1}$$

c_n and c_p are the probability per unit time volume of a hole and an electron being captured by the recombination center. p_s, n_s are free carrier densities on the surface, p_b, n_b, are bulk carrier densities and p_{s1}, n_{s1} are surface carrier densities where the Fermi energy is at the E_i. The energy diagram for this type of recombination is given in figure 3.1.

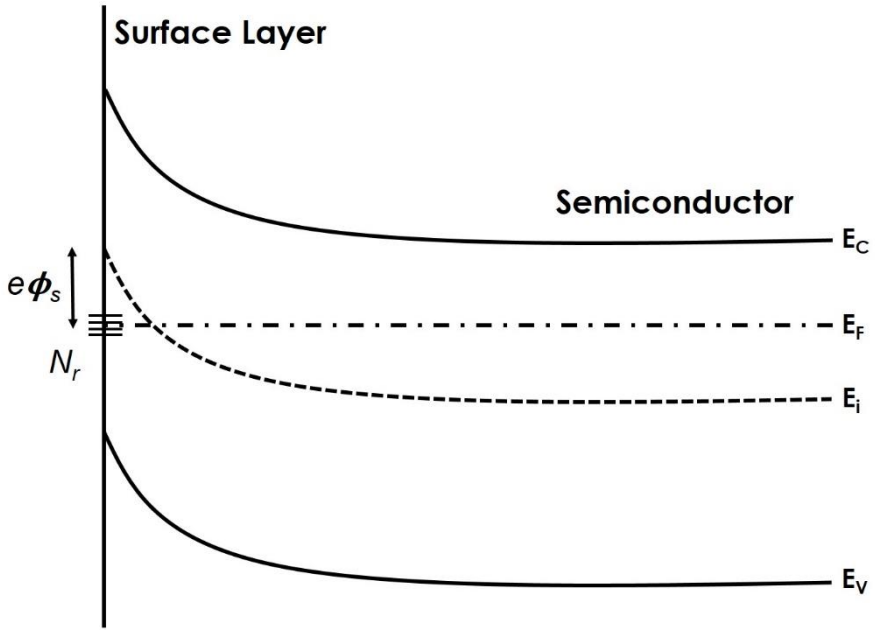


Figure 3.1. Surface state energy level below the mid-gap for an n-type semiconductor.

Assuming that $p_s = p_b$, $n_b = n_s$, the surface recombination rate using equation 3.1,

$$S = \frac{r_s}{\Delta p} = \frac{N_T c_p c_n (p_b + n_b)}{n_i c_n \, exp\left[\frac{E_F - E_i + e\phi_s}{k_B T}\right] + n_i c_p \exp\left[-\frac{E_F - E_i + e\phi_s}{k_B T}\right]} \tag{3.2}$$

Shockley-Read-Hall explains the above formula, and it only applies to a recombination center with a single energy level [22]. The validity of this formula is studied by Gräfe (1971), and he concluded that it is merely a simple model for the highly complicated case; thus, it is only useful to a certain extent [23].

Surface recombination is one of the critical parameters determining the performance of a detector. Especially for the cases where the surface area is comparable with the effective pixel active area, the dark current of the fabricated detector is very likely to be dominated by the surface leakage. The standard method to prevent this is to employ a passivating layer on the surface. Even though the passivation layer is reasonable for covering dangling bonds, surface conditions are still dominant for determining the performance of the detectors for the typical pitch sizes less than 40 μm.

A relatively less discussed topic in surface passivation is the fixed charges on the surface of a detector. An accumulation layer forms at the surface by employing a passivation layer. This accumulation layer is expected to reduce the surface recombination rate and improve the device's performance. Besides, due to the larger conductive area (especially for mesa structures), the devices' resistance and detectivity are degraded. Thus, planar-type photodetectors are employed to decrease the surface area instead of mesa etched photodetectors.

Assuming a photoconductive detector with identical top and bottom surfaces, the resistance of the detector can be approximated as

$$R = \frac{1}{q * (N_b \mu_{\mathrm{b}} + 2N_s \mu_s / d)} \frac{l}{wd}, \tag{3.3}$$

l, w, and d are the detector's length, width, and heigh. N_b, N_s are the bulk carrier density and fixed surface charge density, μ_{b}, μ_s, mobility of the bulk carriers, and surface carrier velocity. Using equation 3.3, one can see the effect of the fixed charges on the resistance of a detector in figure 3.2.

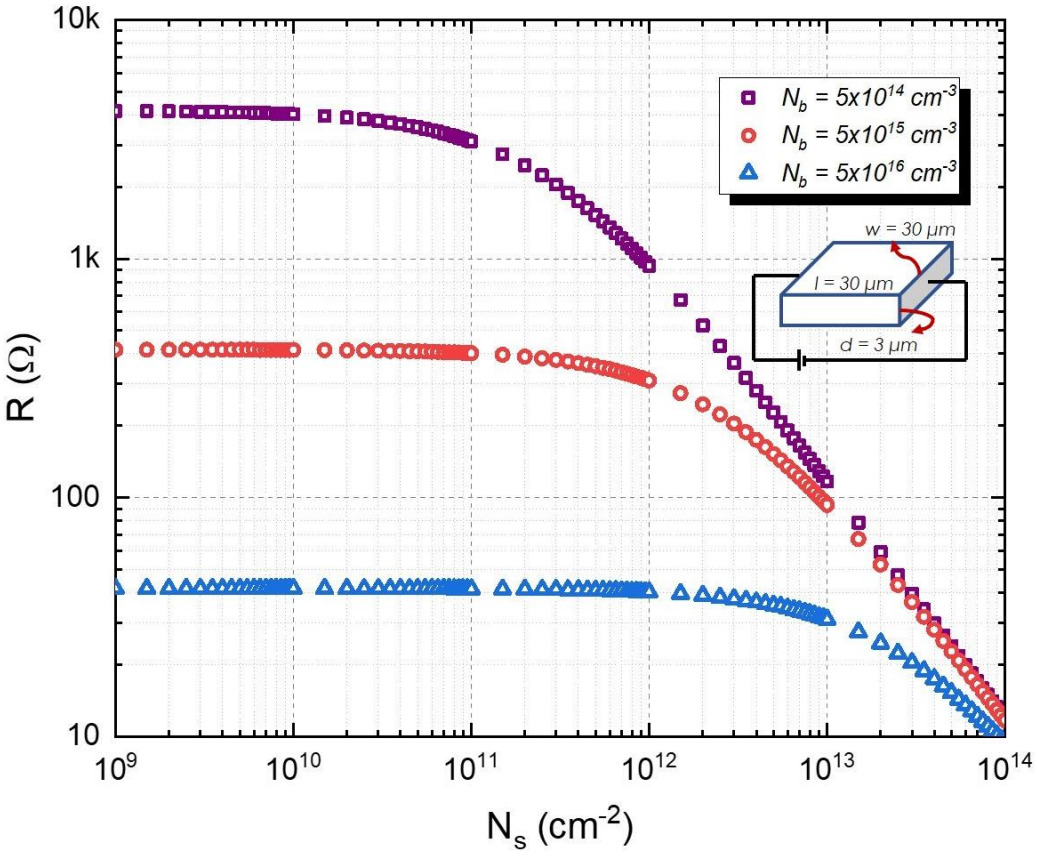


Figure 3.2. Device resistance vs. surface charge densities for various bulk carrier densities of a photoconductor. Derived using equation 3.3. (Used parameters l = 30 μm, w = 30 μm, d = 3 μm. N_b denotes bulk carrier density, N_s denotes surface charge density. The other required parameters are used given in table 2.1.) A similar study for an MCT photoconductive detector is published in ref.: [21].

One way to change the surface fixed charges is to provide a constant electric field to the surface. For this purpose, a metal-oxide-semiconductor (MOS) structure is proposed to change the fixed charge density at the surface by applying a biasing voltage. A representative sketch of this structure is given in figure 3.3.

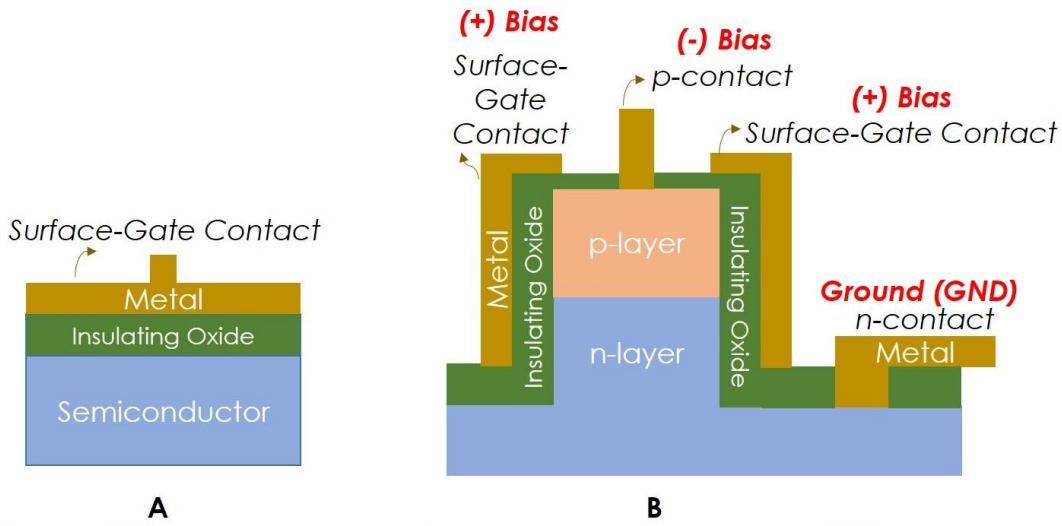


Figure 3.3. Simplified sketches of (A) metal oxide semiconductor (MOS) and (B) suggested structure.

The resultant structure is somewhat similar to the metal-oxide-semiconductor field-effect-transistors (MOSFET). Changing surface-gate–ground voltage can induce a conductive path or block the conductive path depending on the biasing voltage polarity similar to the MOSFETs. The operation point of the detector can be optimized by changing the surface charges adaptively, which is why this is named active surface passivation.

3.2 Fabrication of the Test Detector

The fabrication procedure consists of many micro-fabrication steps followed by material growth. InGaAs/InP epilayers are grown on a 4” InP wafer using the MBE system at the Quantum Devices and Nanophotonics Research Laboratory, METU. Mesa structure with 30 μm pitch is processed on the grown material in the cleanroom. The detailed processing steps and basics of MBE growth are discussed in this section.

3.2.1 Basics of Molecular Beam Epitaxy

Molecular beam epitaxy is a method for epitaxial growth. With several molecular or atomic beams interacting at the surface of a heated substrate, epitaxial growth is achieved in a controlled environment.

An MBE system typically consists of three different chambers to conveniently load-unload substrates without disturbing growth conditions. The load-lock chamber where the samples are loaded and unloaded is divided by the buffer chamber to prevent breaking the ultra-high-vacuum (typical pressures around 1E-11 Torr) at the growth chamber. Each chamber is continuously pumped to avoid any contamination to the growth chamber.

The ultra-high-vacuum condition provides materials with outstanding purity levels. This condition is achieved by pumping the growth chamber with a cryopump and cooling the chamber walls with liquid nitrogen. In-situ mass spectroscopy is used for probing vacuum leaks and determining the impurity molecules inside the growth chamber. On top of that, it requires regular maintenance to keep these conditions which should be carried out diligently since it has many complex parts and modules. A sketch of a common MBE growth chamber is illustrated in figure 3.4.

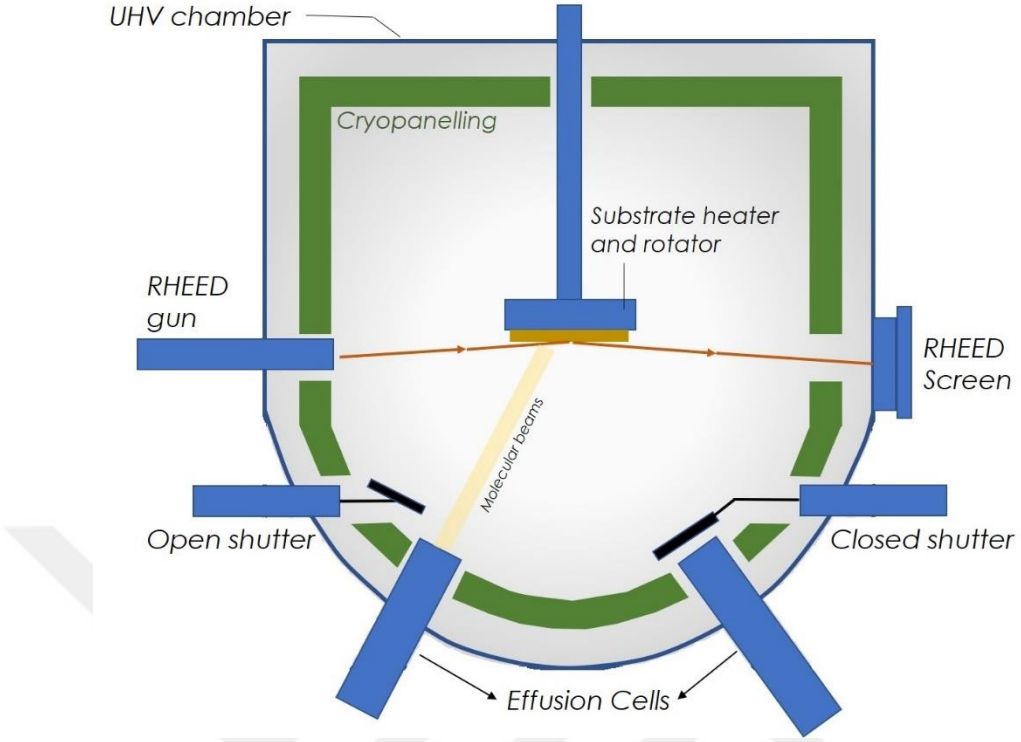


Figure 3.4. A representative sketch of the growth chamber of the MBE reactor.

The growth chamber is equipped with several Knudson effusion cells, a reflection high-energy electron diffraction (RHEED) gun, and a luminant window to monitor the RHEED pattern. Additionally, in-situ mass spectrometry and a rotating substrate holder with a temperature manipulator reside in the growth chamber.

Researchers at Princeton University developed a state-of-the-art MBE system with four cryopumps running simultaneously. They achieved the growth of gallium-arsenide (GaAs) epilayers with unprecedented purity levels. The grown GaAs quantum-well epilayers have only one residual impurity for every 10^{10} Ga/As atoms or the impurity density equivalent of $1x10^{13}$ cm^{-3} with ultra-high mobility of $44x10^{6}$ $V^{-1}s^{-1}$ [24].

With the mentioned conditions provided, evaporated molecules/atoms hit the substrate without interacting with other molecules on their way as if they were laser beams. During the growth, careful temperature manipulations should be made by observing the RHEED pattern to provide the optimum growth conditions. Typical

growth conditions provide a rate of ~1 μm/hour of epilayer growth. The effusion cell shutters switch approximately 0.1 seconds, much shorter than growing a monolayer (typically 1-5 s). Thus, MBE enables the growth of detectors with very thin epilayer structures, such as quantum-well infrared detectors, barrier type (nBn) detectors, and type-II superlattice detectors. The grown epilayer structure for this thesis work is provided in figure 3.5.



Figure 3.5. MBE grown epilayer of the photodetector.

$In_xGa_{1-x}As$ with a mole fraction of x=0.53 epilayer is lattice-matched to the InP substrate. This property of $In_{0.53}Ga_{0.47}As$ enables the growth of high-quality photodetector epilayers with a cut-off wavelength of 1.69 μm. For the ohmic n and p contacts, epilayers with doping densities of 10^{18} cm^{-3} were grown with impurity dopants Silicon (Si) and Beryllium (Be). The Si-doped absorber layer with 3 μm thickness and doping density of $5x10^{16}$ cm^{-3} was grown and optimized for the SWIR applications in Quantum Devices and Nanophotonics Research Laboratory (KANAL).

3.2.2 Processing of Test Detector

Processing of the test detector includes all of the steps after the material growth, up to device measurements. Various microfabrication steps are followed, with a total of five different photolithography masks are used for this test detector fabrication; an

additional photolithography mask is needed for if one wants to have a complete FPA process.

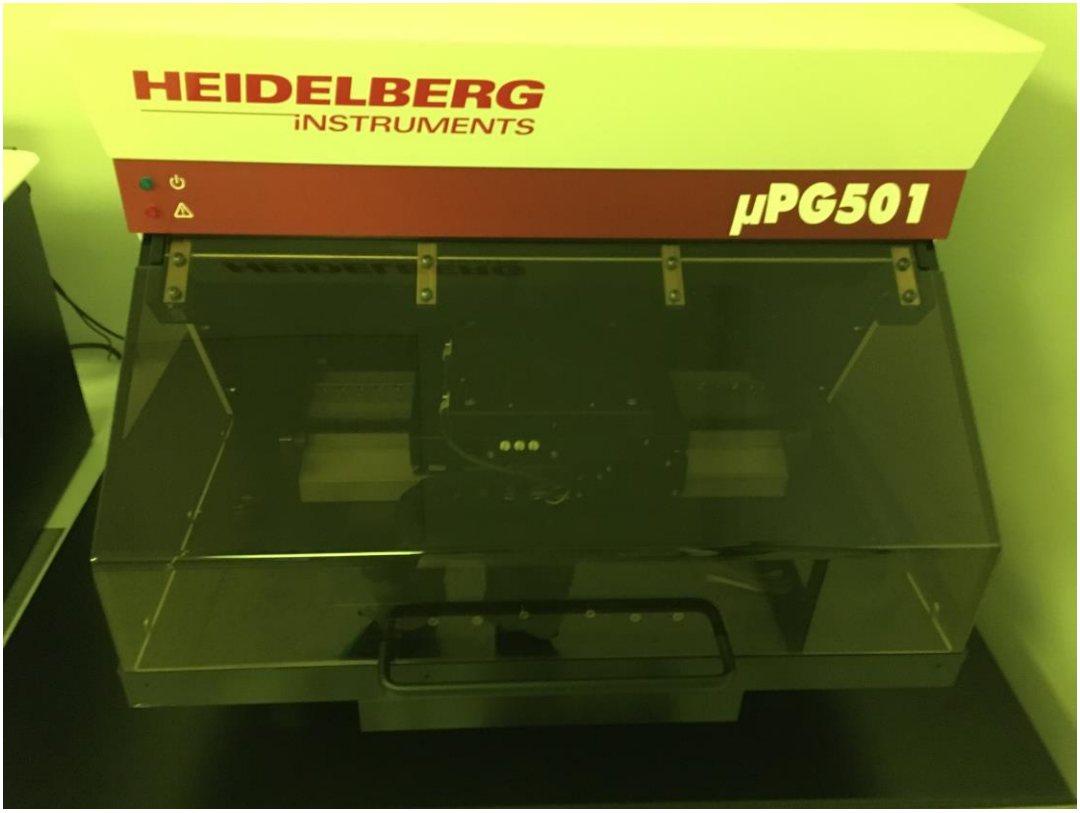


Figure 3.6. μPG 501 – Direct Writer system made by Heidelberg Instruments. METU - Quantum Devices and Nanophotonics Research Laboratory.

Heidelberg μPG 501 – Direct Writer system was used to expose desired patterns using various AZ-series photoresists. A photo of the direct writer is included in figure 3.6. Univex–Leybold Thermal Evaporator system was used for metal coatings. Mesa etching was done with wet etching techniques using a Br-based acid solution. The simplified process flow is given in figure 3.7.

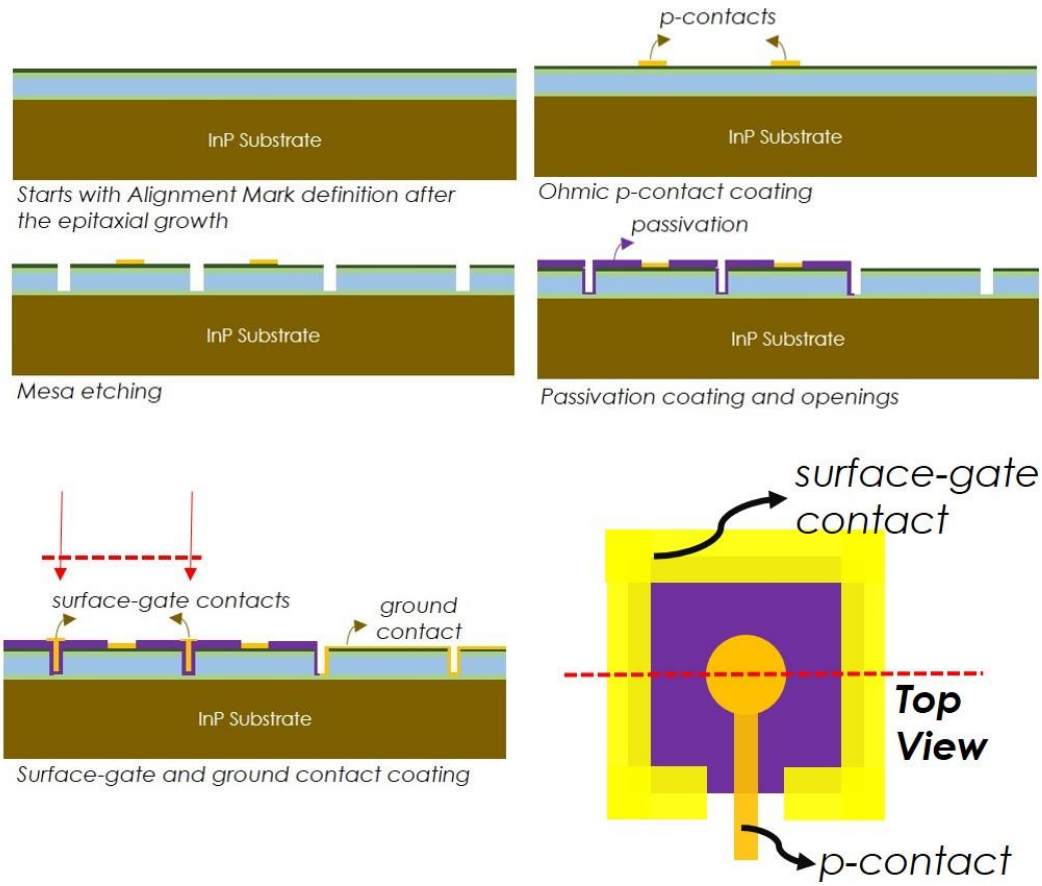


Figure 3.7. Simplified process flow of the fabrication. Given *colors* representing *gold*: contacts, *violet*: passivation, *brown*: substrate, *blue/green*: epilayers.

First, the alignment marks are defined, than the pattern is etched on the sample with wet etching, using a Br-based solution. Next, p-contacts are defined, and Titanium/Gold (Ti/Au) metal layer is deposited with the thermal evaporator and lifted off using a negative AZ-nLoff photoresist. Mesa etching of ~3.5 – 4.0 μm thickness was etched with 30 μm pitch length, and an insulating layer with a thickness of ~800 nm was spin-coated. A scanning-electron-microscope (SEM) image of a sample after mesa etching is given in figure 3.8.

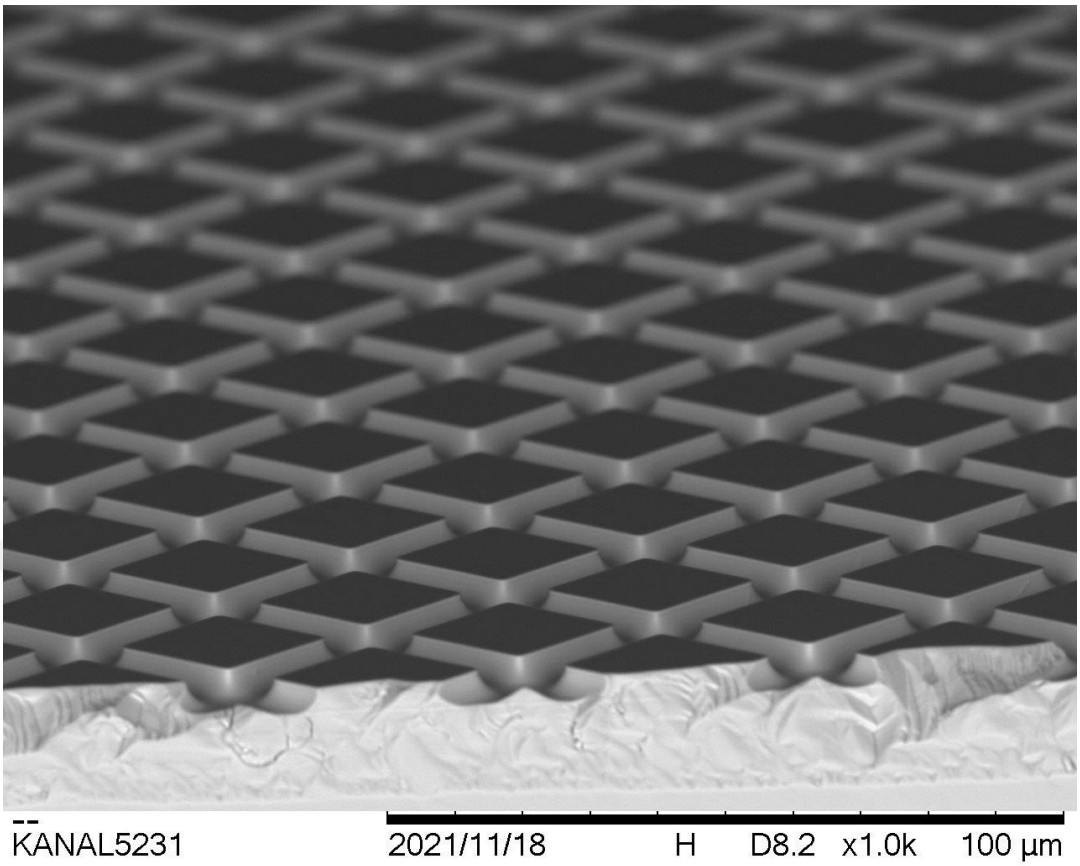


Figure 3.8. Scanning-electron-microscope (SEM) image of a sample after the mesa etching.

The pattern of Surface-Gate, Ground (n-contact), and metal pads for measurement are defined after passivation layer openings, and a Ti/Au metal layer is deposited using the thermal evaporator system. A snapshot of the processed test detector under the optical microscope is shown in figure 3.9.

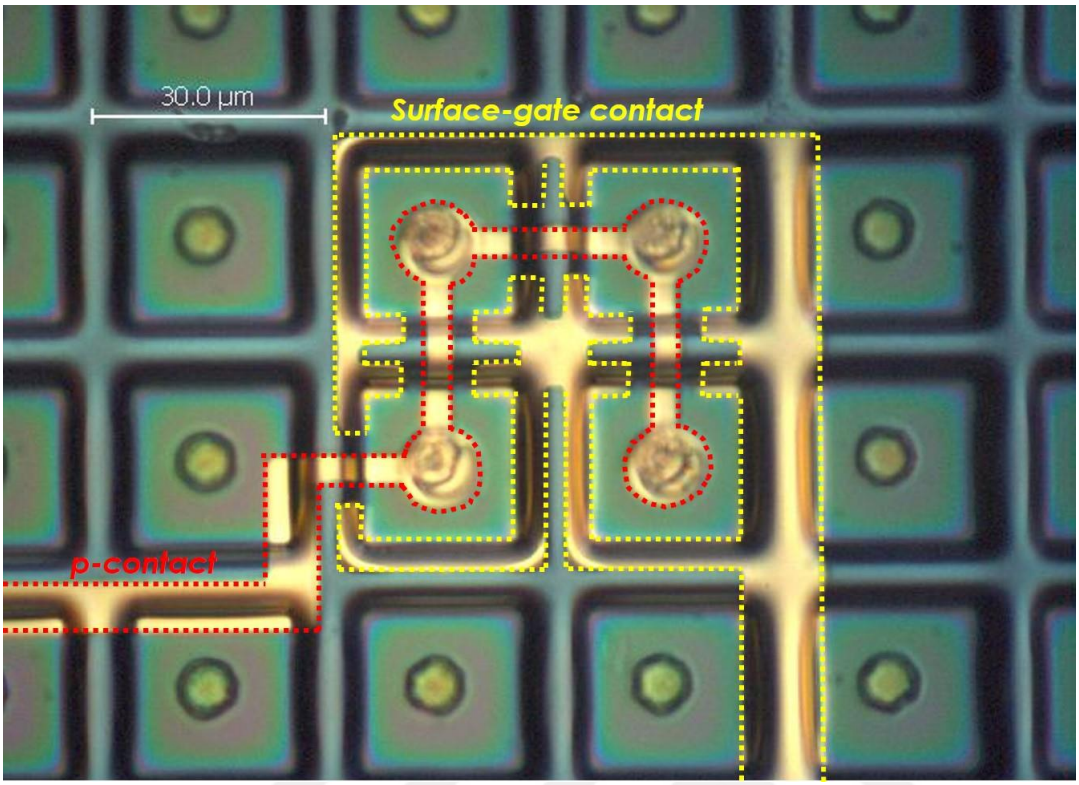


Figure 3.9. Detector image under an optical microscope with 100x zoom. Metal paths of surface-gate contact (yellow) and p-contact (red) are marked with dashed lines.

After completing the microfabrication processes at the cleanroom, the detector was attached to an alumina base with a thermally conductive compound. At this point, the detector is ready to be measured after wire bonding. The snapshots of the last mask layer used in microfabrication and the final detector under an optical microscope are given in figure 3.10 and figure 3.11, respectively.

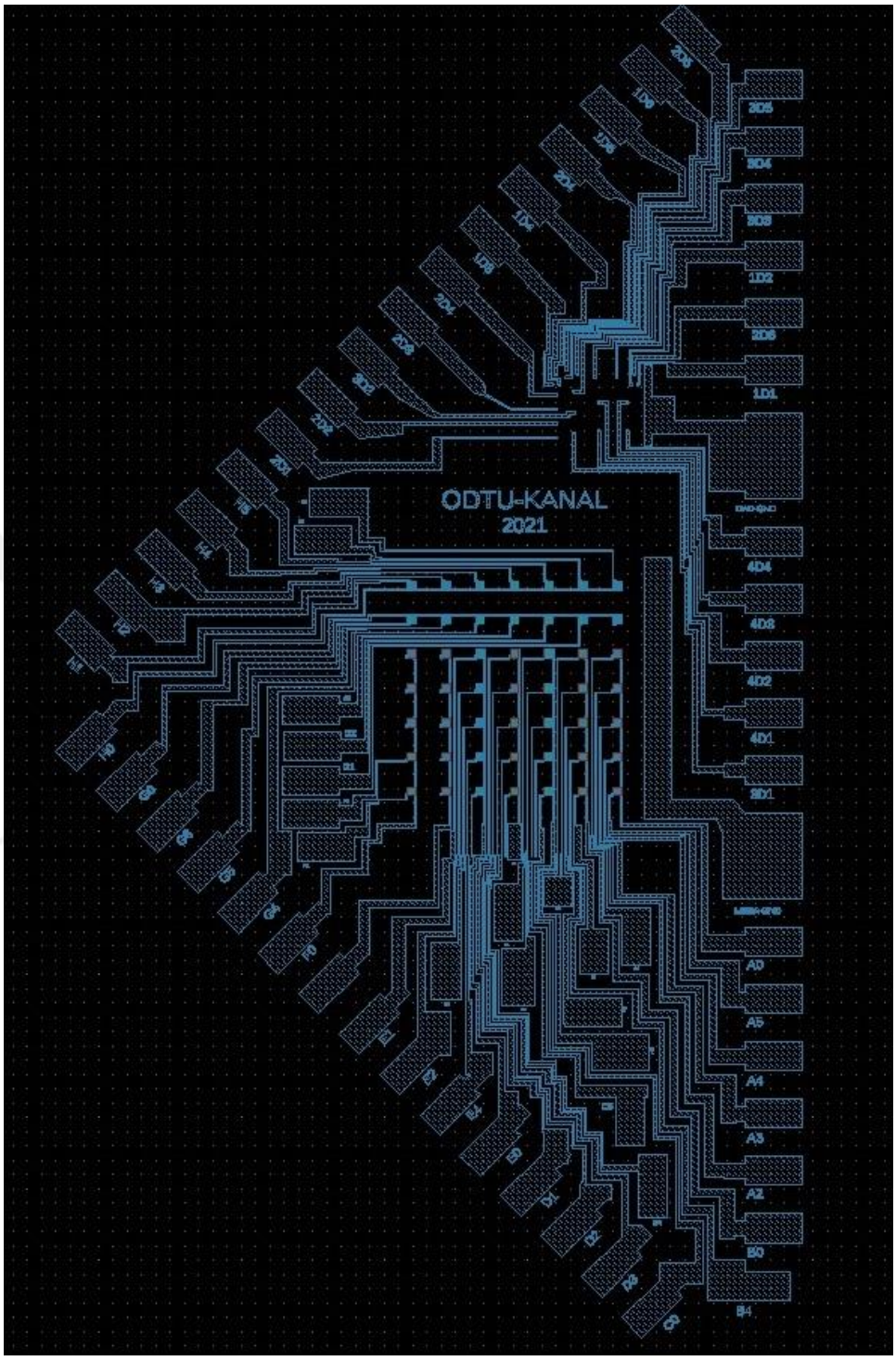


Figure 3.10. The last metal mask was used in the SWIR photodetector process.

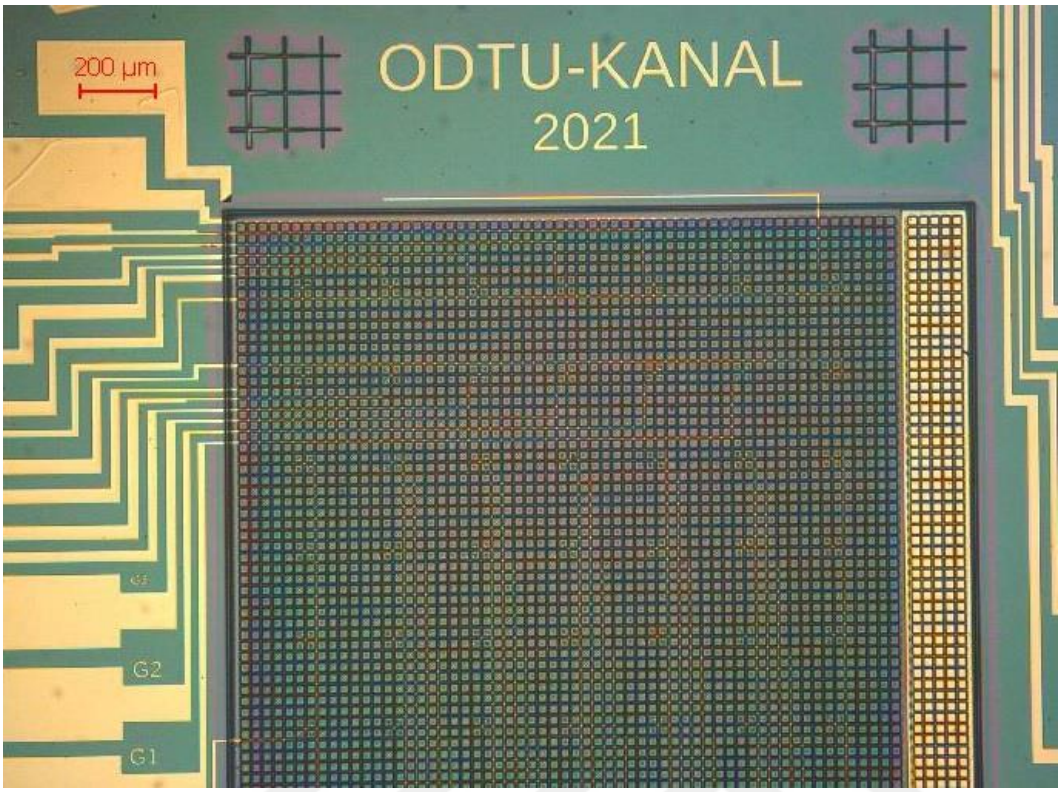


Figure 3.11. Snapshot of the final detector under an optical microscope with 5x zoom.

3.3 Test Detector Characterization and Modelling

The listed figure of merits in chapter 1 is investigated to inspect the detector's performance. The dark current is one of the critical parameters determining the detector's performance. The lower dark current results in a higher signal-to-noise ratio, given that noise of the detector is in the sensible ranges. Responsivity and quantum efficiency are also important parameters for verifying the detector's operation; however, it mainly depends on design parameters such as active layer thickness and mole fraction (x) of compound materials reasonably controllable with the given growth settings. On the other hand, the dark current of a photodetector is determined with controllable parameters such as doping densities and relatively less controllable parameters depending on non-ideal growth conditions (which is

inevitable) and effects of the processing of the detector. Moreover, the noise of the detector and the effect on detectivity is discussed in this chapter.

Please note that the purpose of this work is to verify the proposed method; thus, the performance parameters are reviewed as relative performance improvements rather than ultimately attaining to the state of the are performance.

3.3.1 Responsivity and Quantum Efficiency Measurement

Responsivity/quantum efficiency measurement was made to verify the detector operation. The measurement setup is illustrated in figure 3.12.

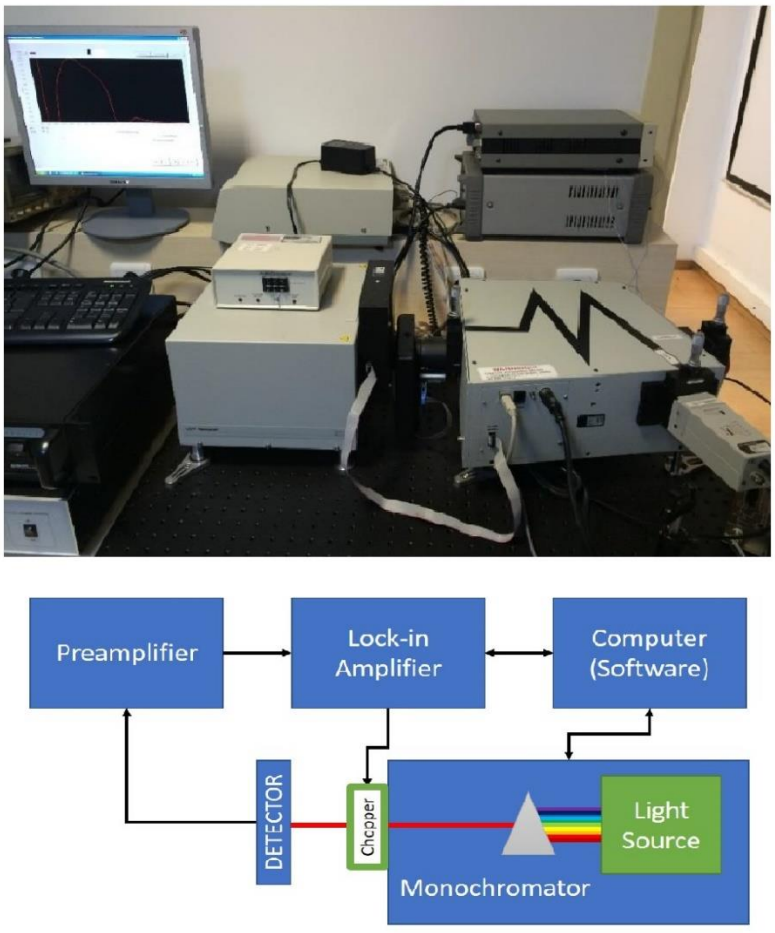


Figure 3.12. Responsivity measurement setup (top) and representative schematic (bottom).

The responsivity measurement setup consists of a monochromator, a lock-in amplifier, and a computer to control the instruments. The monochromator is a mechanical device that controls the output wavelength via moving/rotating the gratings inside. Furthermore, the exiting wavelength is modulated with a chopper, a rotating circular plate with openings to excite the photodetector. This creates an amplitude modulation on the incoming photons. The detector is connected to a low noise transconductance preamplifier to convert the output signal to voltage. The resultant voltage variation is resolved using a lock-in amplifier.

Test detector placed on alumina base is measured with the given setup. Illumination is provided from the substrate side of the detector.

The measured raw data merely correlates the responsivity with the measured voltage output. A calibrated Indium-Arsenide (InAs) photodetector made by Teledyne Judson Technologies is measured as a reference detector to convert the raw data to actual responsivity. With the known responsivity of the reference detector, the raw data is converted to the actual responsivity of the photodetector. Moreover, additional correction terms should be applied to this measurement to get the actual responsivity spectrum.

Such correction terms include; diffusion length, equivalent active area (due to processing), Fresnel reflections from the substrate, and the filtering effect of the alumina base. Due to the diffusion length of the material, carriers generated outside the measured pixels are swept to the contacts with applied bias, increasing the effective measured pixel area. In contrast, the employed wet etching technique decreases the active pixel area. The diffusion length is estimated to be $\sim$32–34 μm with the photocurrent I-V measurements of different area test pixels, and the effective pixel size is measured $\sim$26 μm with an optical microscope. The effect of Fresnel reflection can be understood with equations 1.13 and 1.15, which are caused by the refractive index mismatch. The transmission of the alumina base is measured with additional measurements using the reference detector. The responsivity of the detector is given in figure 3.13.

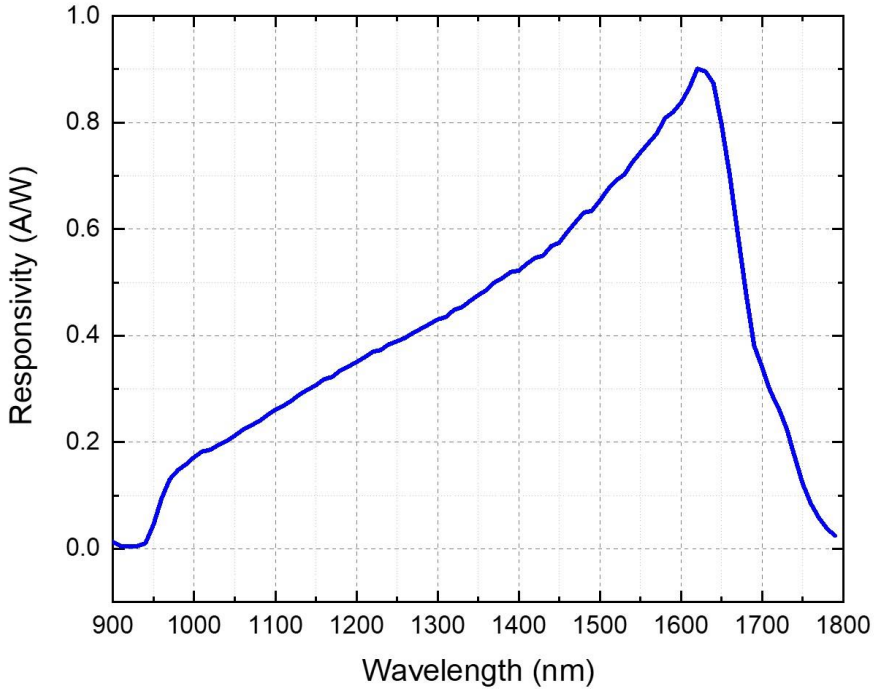


Figure 3.13. The responsivity of the photodetector. The sample is illuminated from the backside. InP substrate with a thickness of 800 μm was not thinned down. Calibrated InAs detector is used as a reference detector.

3.3.2 Dark Current Measurements and Modelling

I-V measurements are made by sweeping p-n junction terminal voltages for varying surface-gate voltages. As it is illustrated in figure 3.3, the surface-gate terminal is connected to the (+) bias, the n-contact terminal to ground (GND), and the p-contact terminal to (-) bias. The measurement result at 300 K temperature is given in figure 3.14. It is observed that photocurrent does not change for different applied surface-gate voltages for constant arbitrary illumination. Assuming the MOS structure as a parallel plate capacitor, applied voltage per insulator layer thickness is given with the unit of V/μm for convenience; since it is highly dependent on insulator layer thickness.

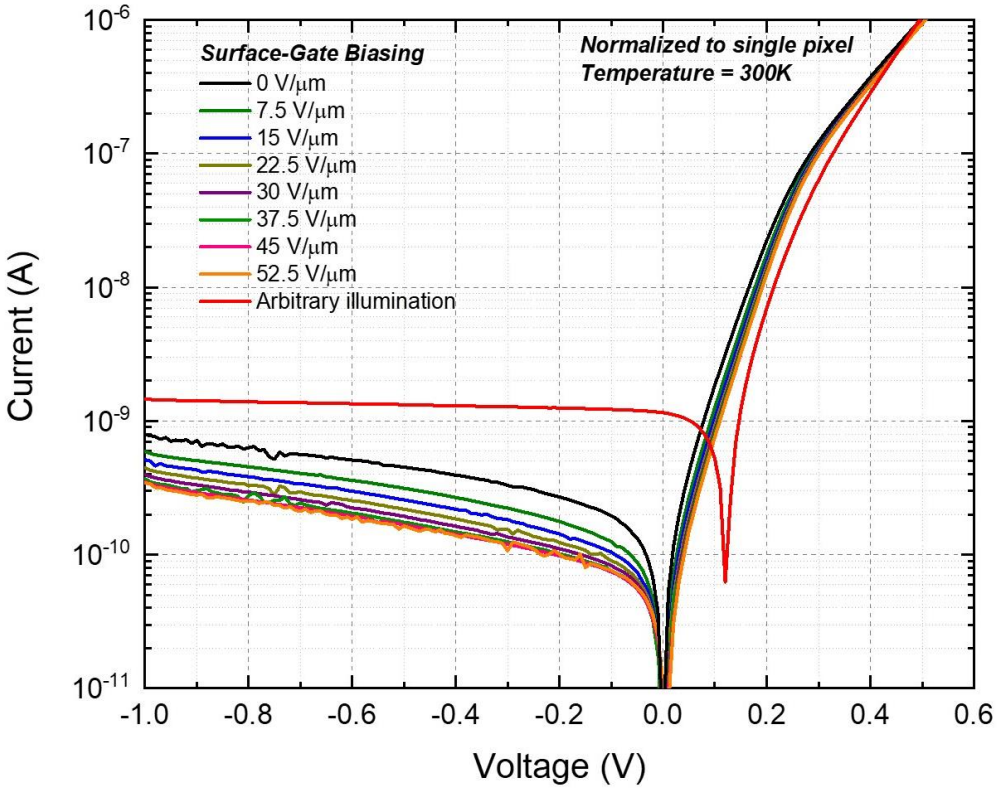


Figure 3.14. Dark current IV graph for various surface-gate biases with pn-junction terminal biasing voltage swept from -1 to 0.6 V at 300 K.

The effect of surface-gate biasing on the IV measurement can be observed in above figure 3.16. The dark current is 176 pA at -0.1 V with zero surface-gate biasing condition. Whereas for 52.5 V/μm surface-gate biasing, the dark current of a pixel is decreased to 71 pA at -0.1 V. This result suggests an improvement of ~2.5 times in the dark current of the photodetector at 300 K temperature. For an arbitrary illumination, photocurrent (total measured illuminated current minus the dark current) is observed to be constant with changing surface-gate biasing; therefore, only a single illuminated measurement is included for the readability of the figure.

Furthermore, the effect of the active surface passivation gradually diminishes for increased surface-gate voltages. To be more explicit, for 30 V/μm surface-gate biasing, the dark current is measured 86 pA at -0.1 V further decreased marginally for 52.5 V/μm surface-gate biasing to 71 pA. Saturating dark current for higher

surface-gate biasing may indicate that the effect of the active surface passivation acts on a particular dark current mechanism rather than simultaneously affecting all dark current mechanisms. In other words, by suppressing some particular dark current mechanism, other dark current mechanisms become dominant. It is further studied by dark current modeling.

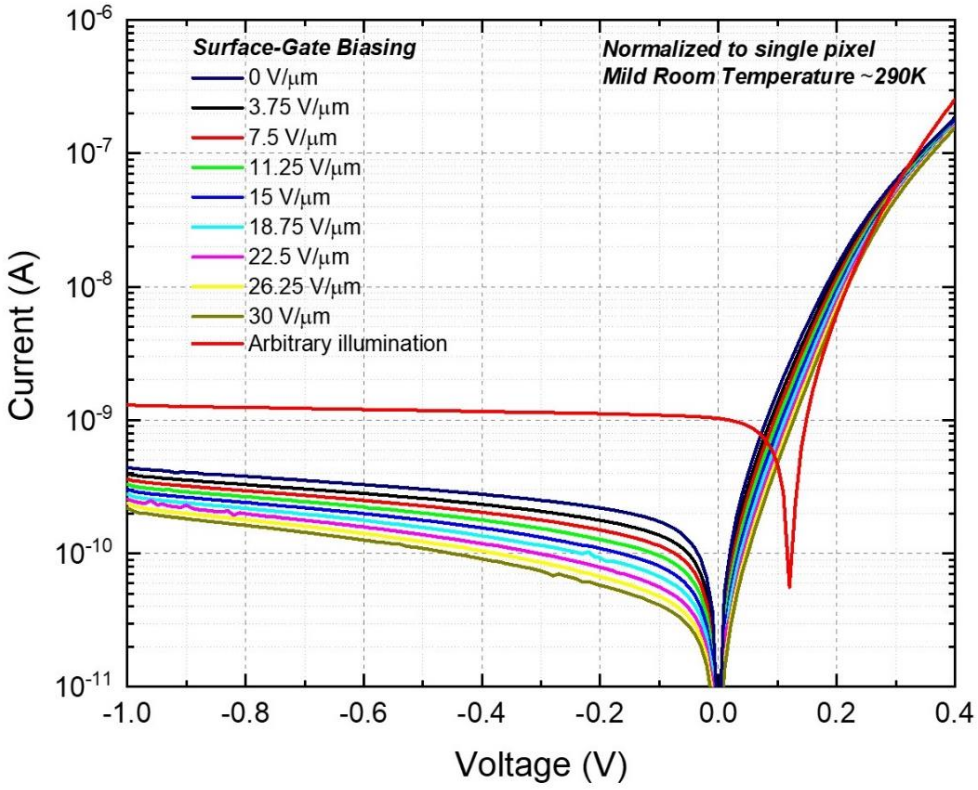


Figure 3.15. Dark current IV graph for various surface-gate biases with pn-junction terminal biasing voltage swept from -1 to 0.4 V at mild room temperature.

The dark current IV measurement at the mild room temperature is given in above figure 3.15. Similar to the 300 K case, a decrease in the dark current is observed with inducing surface-gate biasing. 173 pA per pixel is measured for zero surface-gate bias with -0.1 V pn-junction biasing. Dark current is decreased to 40 pA per pixel for 30 V/μm surface-gate bias, which indicates more than four times improvement in the dark current of the photodetector. Similar to the previous case, saturation effect is observed in dark current with increasing surface-gate biasing; namely, 46 pA for

26.25 V/μm surface-gate bias, 40 pA for 30 V/μm surface-gate bias where the rate of change in dark current is much lower compared to the lower surface-gate bias voltages.

Additionally, one can argue that the slope of the reverse saturation current changes with inducing different surface-gate biases at higher reverse terminal biasing. It may indicate that the trap-assisted tunneling (TAT) current becomes dominant due to suppressing other dark current mechanisms. These claims are investigated via modeling the dark current mechanisms.

In order to model the dark currents given by figures 3.14 and 3.15, the following equations can be used:

$$I_{diff} = C_{diff}(e^{qV/k_BT} - 1), \tag{3.13}$$

$$I_{g-r} = C_{g-r}\sqrt{V_{bi} - V}\left(e^{\frac{qV}{2k_BT}} - 1\right), \tag{3.14}$$

$$I_{shunt} = C_{shunt}V. \tag{3.15}$$

C_{diff}, C_{g-r} and C_{shunt} parameters defined in equations 3.13, 3.14, and 3.15 are obtained by replacing the non-voltage dependant parameters given in equations 1.13, 1.18, and 1.21. These parameters can be found by using a curve-fitting algorithm. While doing the curve-fitting, the important point is administering the parameters to have meaningful results. The curve-fitting algorithm tends to be stuck at the local minima if one gives full control to the algorithm over the parameters. Although defining reasonable ranges for the parameters is enough most of the time, it may still get stuck to the limits of the ranges. Another point is to watch over whether to do over-parametrization or under-parametrization. Iteratively managing the parameters is the best way to keep the algorithm in check, and visual aid of the fitted functions is also helpful.

As a rule of thumb, the decision to include a parameter is made if included parameter improves the fit quality by at least 10%. Most algorithms employ the mean-square error rate (R^2) to determine the fit quality. These algorithms generally converge by

reaching a desired R^2 value or simply diverge. If it diverges, the scenario is very likely that either the defined functions are not good enough to determine the characteristic of the input or the defined ranges of the parameters are not valid. The dark current modeling of the experimental results is carried out diligently considering these points.

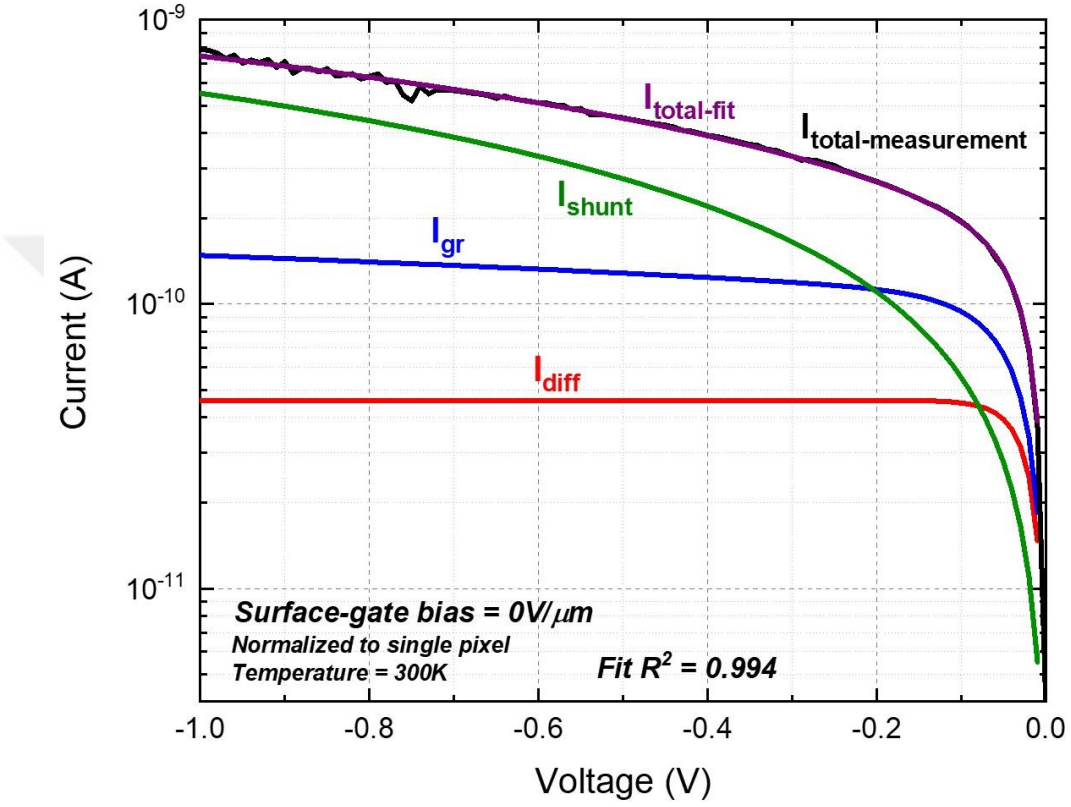


Figure 3.16. IV modeling of the experimental result for zero surface-gate biasing case at 300 K.

The dark current modeling for the zero surface-gate biasing at 300 K is given in figure 3.16. It can be observed that the device characteristic is limited to GR current up to -0.2 V and to shunt current for the rest. The detailed fitting parameters are given in table 3.2.

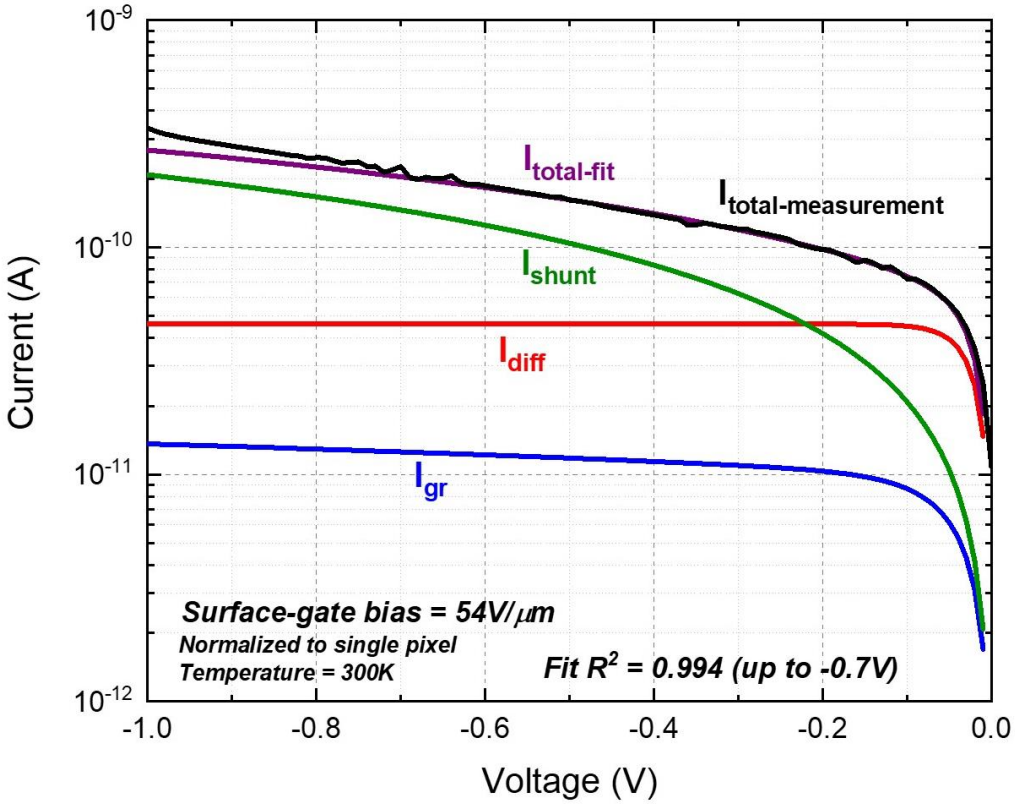


Figure 3.17. IV modeling of the experimental result for 54 V/μm surface-gate biasing at 300 K.

The dark current modeling of the experimental data of 54 V/μm applied surface-gate bias at 300 K is provided in above figure 3.17. It is observed that the dominant mechanism is diffusion current up to -0.2 V bias and shunt current for the rest. It can be seen that GR current is decreased from 94 pA in zero surface-gate biasing case to 8.6 pA in 54 V/μm surface-gate bias at 0.1 V reverse biasing of pn-junction by comparing the figures 3.13 and 3.14. Similarly, the shunt current decreases from 55 pA to 20 pA, whereas the diffusion current stays constant.

It should also be noted that the fitted curve starts diverging after -0.7 V bias due to trap-assisted tunneling (TAT) becoming dominant in that region. It can be said that inducing high enough surface-gate biasing, the device characteristic is determined

with the diffusion current at the -0.1 V operating voltage, which is desirable since the diffusion current is an unavoidable dark current component.

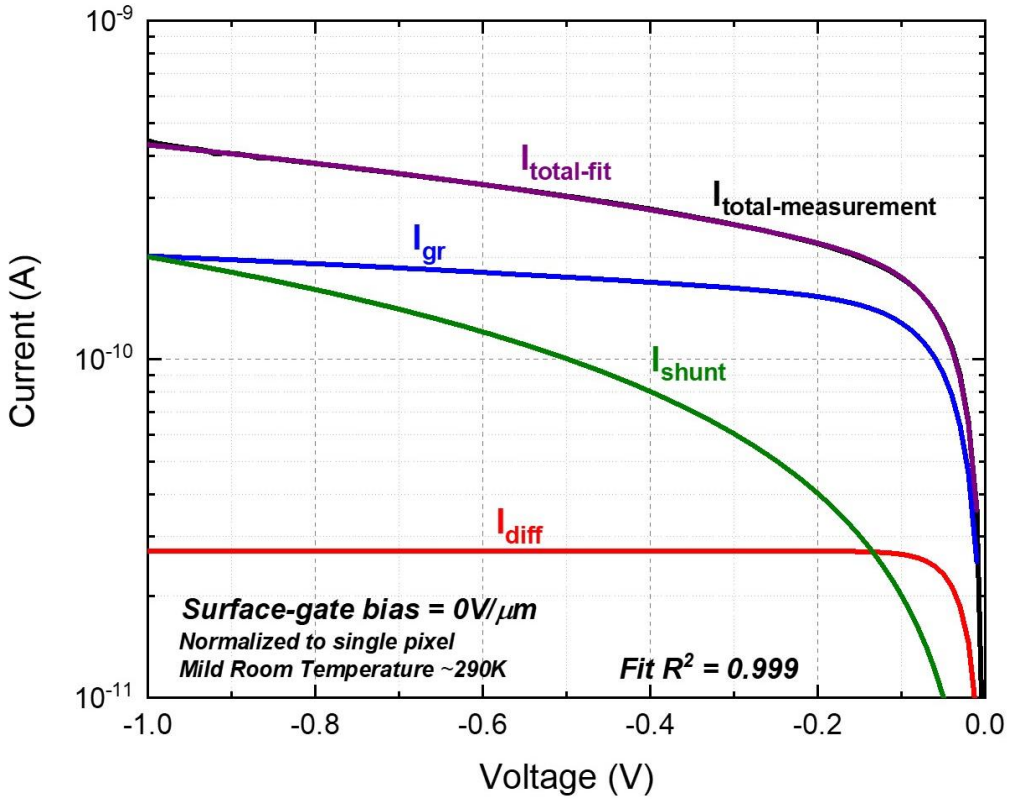


Figure 3.18. IV modeling of the experimental result for zero surface-gate biasing case at mild room temperature.

Modeled dark current components for the experimental measurement at mild room temperature with zero surface-gate biasing is given in figure 3.18. Observed device characteristic is limited with the GR component of the dark current. The reported GR current is 128 pA, and the shunt current is 21 pA at -0.1 V biasing. Divergence from the measured IV due to the TAT is observed around -1 V vaguely.

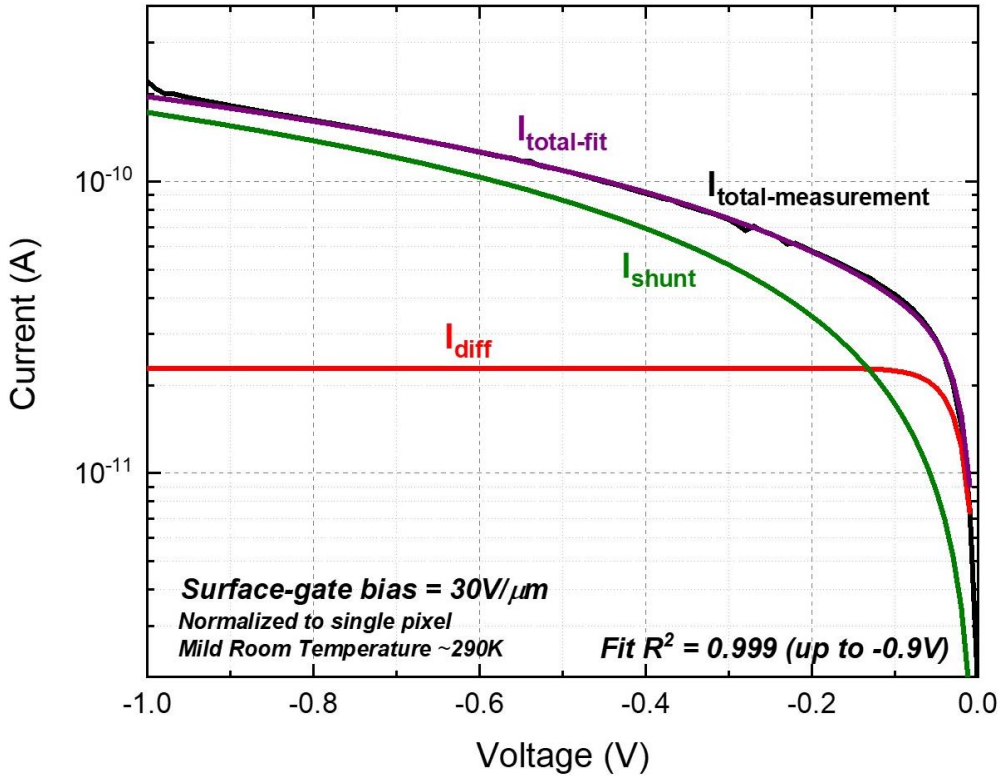


Figure 3.19. IV modeling of the experimental result for 30 V/μm surface-gate biasing at mild room temperature.

With inducing high enough surface-gate biasing at mild room temperature, the modeled IV graph is given in figure 3.19. It is observed that the GR component of the dark current is in the order of error margin, which is said to be a bulk GR component. The error margin is expected to be ten times smaller than the reported diffusion current. Thus, the GR current parameter is not included in this modeling, since the fit quality does not change. The device characteristic is dominated by the diffusion current up to -0.14 V and by the shunt current for the rest. The reported shunt current is 17 pA at -0.1 V.

From figures 3.16 and 3.17, the GR current is reduced significantly by inducing high enough surface-gate bias voltage, numerically 128 pA to an error margin of ~1 pA.

Overall, the total dark current is decreased by roughly 2.5 times at room temperature and more than 4 times at mild room temperature. This result can be explained by the temperature dependence difference of dark current components.

Intrinsic carrier concentration is known to be highly temperature-dependent. The diffusion current is proportional with the n_i^2, whereas the GR current is proportional with the n_i. It is shown that the GR current is decreased by more than 90% for both cases of different temperatures. It is expected that under a lower environment temperature and with high enough surface-gate biasing, the total dark current must decrease more for the lower temperature case. Therefore, the improvement in the total dark current is expected to be higher for the lower temperature by further suppressing the GR current via surface-gate biasing, which is the case.

3.3.3 Differential Resistance and Shunt Resistance

Differential resistance is an important parameter determining the performance of a photodetector. One of the figures of merits: specific detectivity is highly dependent on the noise current of the photodetector. Mainly two dominant noise sources; shot and Johnson noise are crucial while determining the specific detectivity of the SWIR photodetector. The generated photocurrent is expected to be lower than the dark current of the photodetector. Therefore, shot noise is determined with the dark current of the photodetector. In order to calculate Johnson noise, dynamic resistance can be extracted with the following equation 3.16.

$$R_{dynamic} = \frac{dV}{dI} = \frac{\Delta \mathrm{V}}{\Delta \mathrm{I}} \tag{3.16}$$

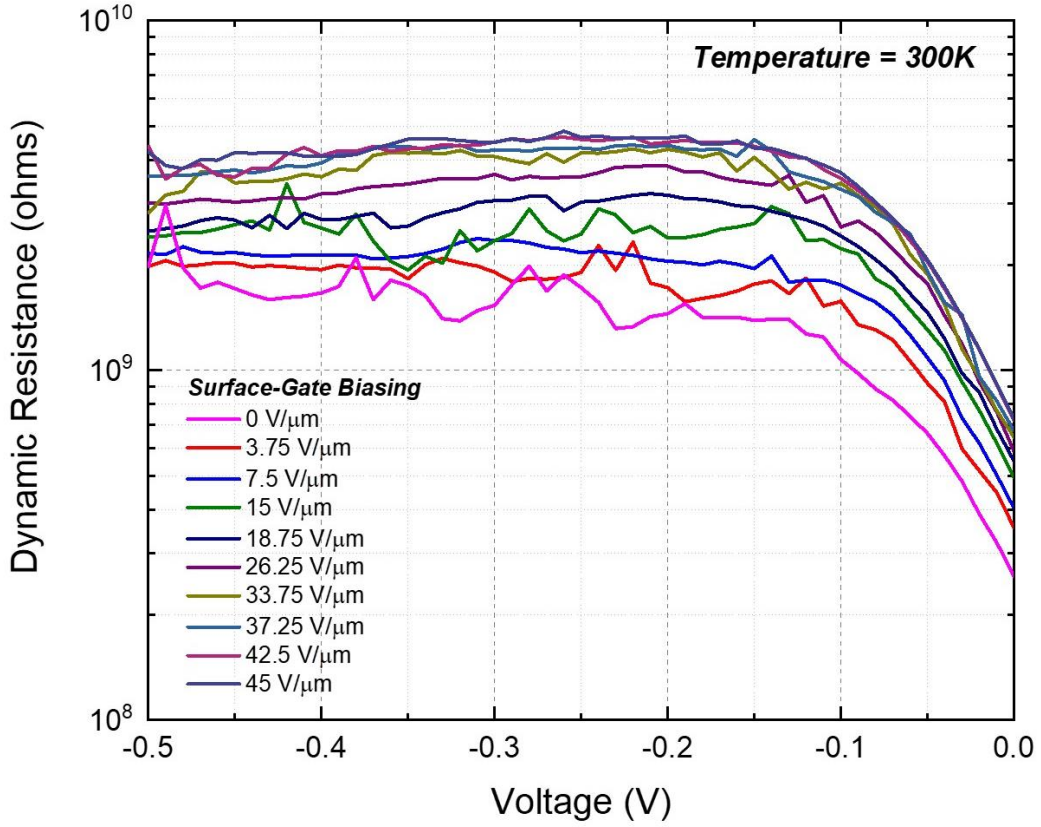


Figure 3.20. Calculated dynamic resistance with given applied surface-gate biasing at 300 K.

Calculated dynamic resistance with equation 3.16 at 300 K is given in figure 3.20. The dynamic resistance of the photodetector is improved 3 times at -0.1 V with inducing a high enough surface-gate bias of 42.5 V/μm. Assuming the noise of the photodetector is limited with the Johnson current, this will translate to $\sqrt{3}$ times improvement to the specific detectivity.

Additionally, for the case of shot noise is limited with the dark current, and given that it is comparable with the Johnson current, the specific detectivity will improve with the mean sum of Johnson and shot noise currents.

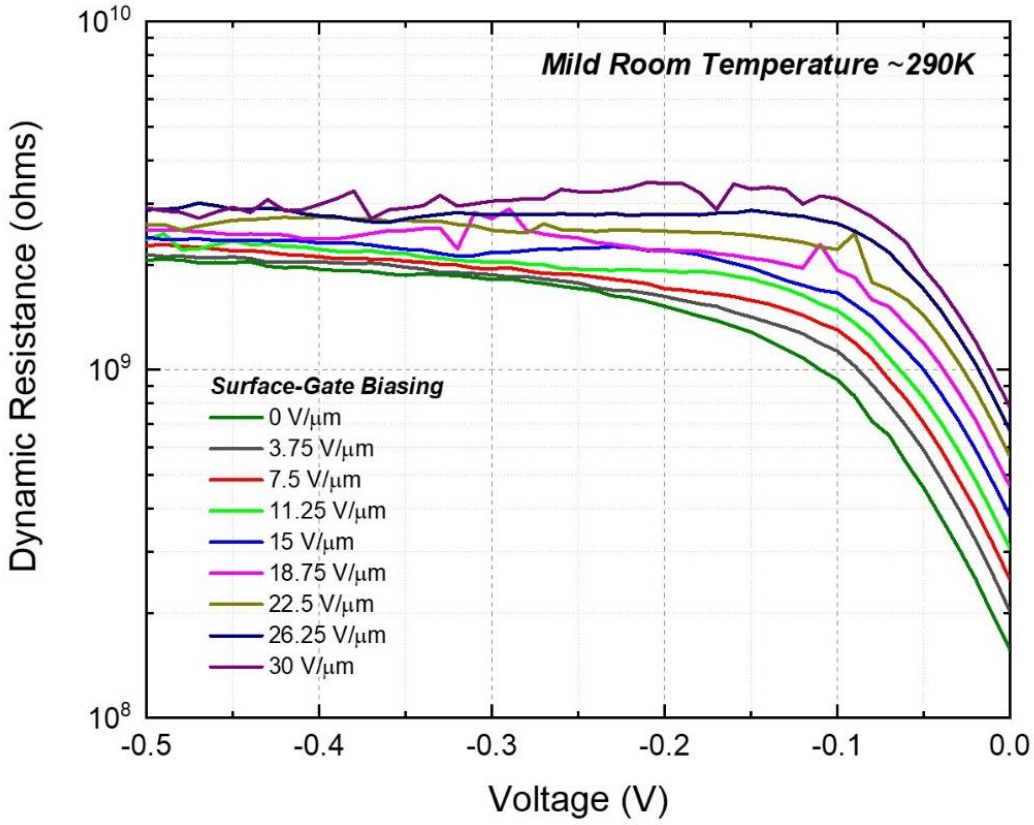


Figure 3.21. Calculated dynamic resistance with given applied surface-gate biasing at mild room temperature.

Dynamic resistance deduced from the dark current measurements is given in figure 3.21 at the mild room temperature case. Similar to the 300 K case, the calculated dynamic resistance is 3 times higher from the zero surface-gate bias at -0.1 V. The zero-bias differential resistance is improved more than 5 times from 0.15 GΩ to 0.78 GΩ.

The insulator (passivation) layer is expected to form an inversion layer on the surface, as shown in figure 3.1. For energy band-bending of $e\phi_s$ the surface electron density is approximated as follows:

$$n_s = N_d e^{-q\phi_s/kt} \tag{3.17}$$

Inducing surface-gate voltage results in energy bending on the surface [49]. For the accumulation mode of the MOS capacitor, electron density at the surface is defined by manipulating equation 3.17:

$$n_s = N_d e^{-q(\phi_s - V_s)/kt} = N_d e^{-q\phi_s/kt} e^{V_{surface-gate}/\tau_{surface}} \quad (3.18)$$

V_s is equivalent band-bending at the surface due to the applied surface-gate voltage. It is estimated using applied surface-gate biasing ($V_{surface-gate}$) and charge generation lifetime ($\tau_{surface}$) at the surface. It is further simplified by denoting constant parameters C_s. Thus, the surface-gate dependent surface charge density is:

$$n_s(V_{surface-gate}) = C_s e^{V_{surface-gate}/\tau_{surface}} \quad (3.19)$$

It can be inferred from equation 3.3 that the shunt resistance is inversely proportional to the surface charge density. Thus, the channel resistance at the surface is:

$$R \propto \frac{1}{n_s} \rightarrow R_{shunt-surface}(V) = R_{shunt-surface} e^{-V_{surface-gate}/\tau_{surface}} \quad (3.20)$$

$R_{shunt-surface}$ corresponds channel resistance of the pixel with zero surface-gate biasing. The total shunt resistance in terms of channel resistance and bulk resistance:

$$R_{shunt,eff} = R_{shunt-surface} \,//\, R_{shunt-bulk} \quad (3.21)$$

$$R_{shunt,eff} = \frac{R_{shunt-bulk} C_{shunt-surface} e^{-V_{surface-gate}/\tau_{surface}}}{R_{shunt-bulk} + C_{shunt-surface} e^{-V_{surface-gate}/\tau_{surface}}} \quad (3.22)$$

Fitting results of the effective shunt resistance for changing surface-gate bias voltage at 300 K are given in figure 3.22.

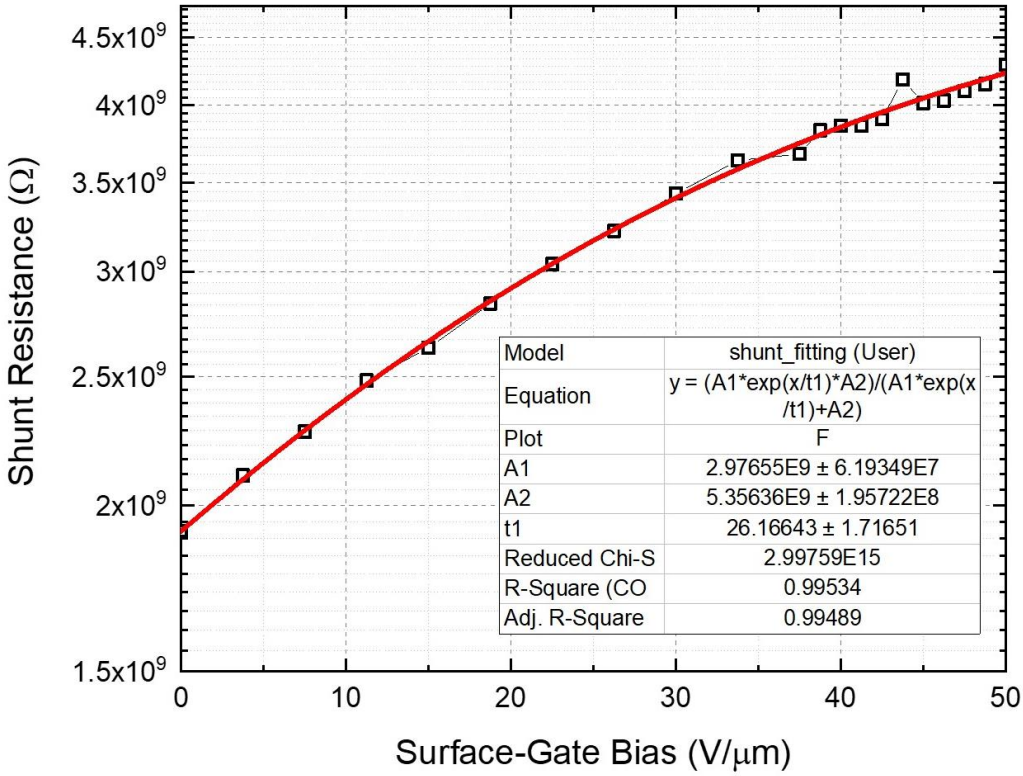


Figure 3.22. Calculated shunt resistances (*black box*) and fitting (*red line*) for various surface-gate biasing at 300 K temperature.

The surface and the bulk component of the shunt resistance is further estimated by fitting the effective shunt resistance data with equation 3.22. The resultant shunt expressions of the device are:

$$R_{shunt,eff} = \frac{5.36 * 2.98 * e^{-\frac{V_{surface-gate}}{26.2 \pm 1.7}}}{5.36 + 2.98 * e^{-\frac{V_{surface-gate}}{26.2 \pm 1.7}}} \ (G\Omega) \tag{3.23}$$

$$R_{shunt-surface} = 2.98\, e^{-\frac{V_{surface-gate}}{26.2 \pm 1.7}} \ G\Omega \tag{3.24}$$

$$R_{shunt-bulk} = 5.36\ G\Omega \tag{3.25}$$

3.3.4 Specific Detectivity and Effective GR Lifetime

Specific detectivity is one of the figures of merits discussed in chapter 1. Assuming that the photocurrent is much lower than the dark current, shot noise can be estimated with the dark current. The specific detectivity is expressed using equations 1.28, 1.31, and 1.34:

$$D^* = \frac{\sqrt{A_d \Delta f}}{i_n} R_i = \frac{\sqrt{A_d \Delta f}}{\sqrt{(i_{n,shot}^2 + i_{n,Johnson}^2)}} R_i \,, \qquad \left(\frac{cm\sqrt{Hz}}{Watt}\right) \tag{3.26}$$

$$D^* = \frac{\sqrt{A_d \Delta f}}{\sqrt{2qI_{tot}\Delta f + \frac{4k_B T \Delta f}{R_{diff}}}} R_i = \frac{\sqrt{A_d}}{\sqrt{2qI_{dark} + \frac{4k_B T}{R_{diff}}}} R_i. \tag{3.27}$$

Plugging experimental data to equation 3.27, specific detectivity at mild room temperature is calculated in table 3.1.

Table 3.1 Calculated figure of merits at mild room temperature. The peak responsivity of 0.9 A/W at 1630 nm wavelength is used.

Surface-Gate Bias	*Dark Current* *($\mu A/cm^{-2}$)*	*Diff. Resistance @ -0.1 V (GΩ)*	*Peak D** *($cm \cdot Hz^{1/2}W^{-1}$)*	*QE* *(%)*
0	4.27	0.93	4.96×10^{11}	70
30 V/μm	0.96	3.10	1×10^{12}	70

The calculated effective GR lifetime at 300 K is given in figure 3.23. Effective GR lifetime is extracted from the experimental results, similar to the figures 3.14-17. The data used is shared in table 3.2.

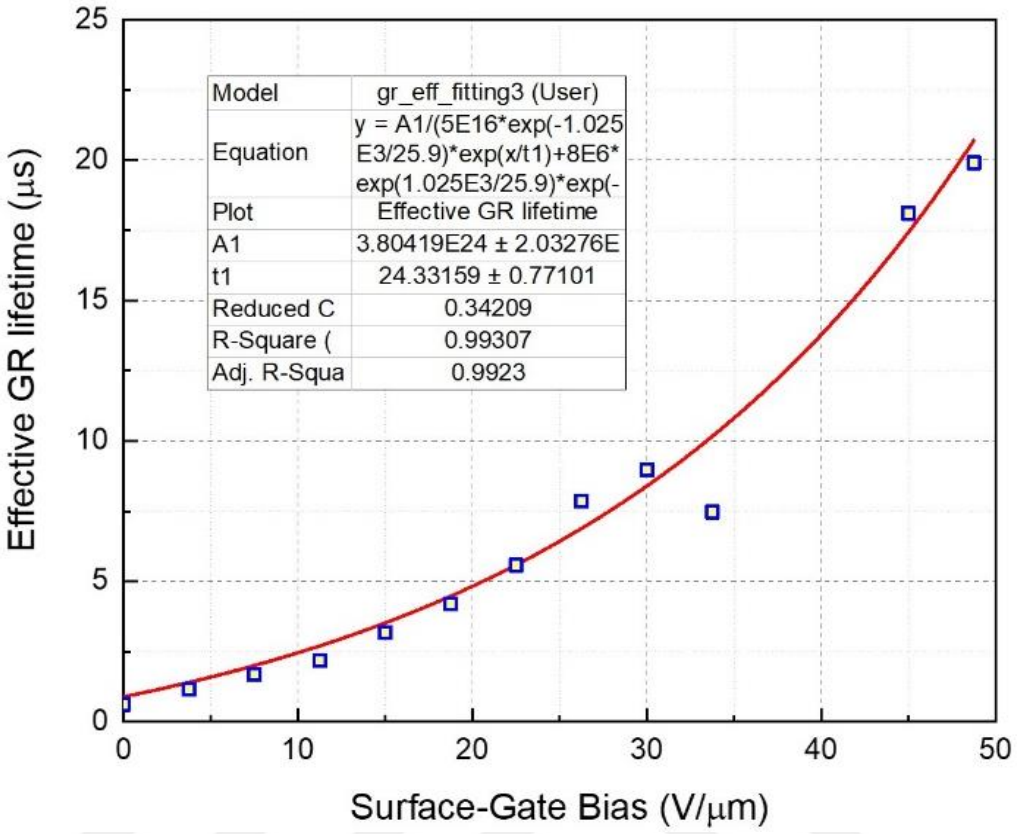


Figure 3.23. Calculated effective GR lifetime for various applied surface-gate voltages at 300 K.

It is observed that the effective GR lifetime ($\tau_{gr,eff}$) equals to 0.6 μs with zero surface biasing. $\tau_{gr,eff}$ is improved 30 times to 20 μs with inducing surface-gate biasing of 48.75 V/μm.

The complete analysis of the GR recombination at the surface is complicated. Let us assume a simple recombination process with a low-level excitation. The recombination lifetime is inversely proportional to surface charge densities [50]. Therefore, voltage-dependent surface GR lifetime is defined with the surface charge dependency denoted by equations 3.17-19. The voltage-dependent surface GR lifetime:

$$\tau_{gr-surface}(V) = \frac{C_{ss}}{(n_0 e^{V_{surface-gate}/\tau_{surface}} + p_0 e^{-V_{surface-gate}/\tau_{surface}})} \quad (3.28)$$

The effective GR lifetime is:

$$\frac{1}{\tau_{gr-eff}} = \frac{1}{\tau_{gr-surface}} + \frac{1}{\tau_{gr-bulk}} \tag{3.29}$$

The equations given in 3.29 and 3.30 are used to fit the estimated effective GR lifetime in figure 3.23. The effective surface GR lifetime in figure 3.23 is expressed:

$$\tau_{gr-surface}(V_{surface-gate}) = 3e^{\frac{V_{surface-gate}}{24.3\pm0.7}} - 2.3\ \mu s. \tag{3.30}$$

Notice that the rate of change of the shunt resistance and the surface GR lifetime can be said to be equal with given error margins. Thus, both improvements in GR and shunt currents are explained with the same mechanism.

Table 3.2 Details of the fitting parameters for the measurement made at 300 K. (C1: C_{diff}, C2: $C_{g\text{-}r}$, C3: C_{shunt} denoted by equations 3.13-15.)

Surface-Gate Bias	**C1**	**C2**	**C3**	**Fit R^2**	**1/C3**	τ_{gr-eff}
V/μm	A	A	S		Ω	μs
0	4.20E-11	1.18E-10	5.23E-10	0.994	1.91E+09	0.61437
3.75	4.20E-11	6.23E-11	4.75E-10	0.999	2.11E+09	1.1599
7.5	4.20E-11	4.31E-11	4.40E-10	0.999	2.27E+09	1.67672
11.25	4.20E-11	3.31E-11	4.03E-10	0.993	2.48E+09	2.18608
15	4.20E-11	2.28E-11	3.81E-10	0.999	2.63E+09	3.16608
18.75	4.20E-11	1.72E-11	3.52E-10	0.998	2.84E+09	4.19717
22.5	4.20E-11	1.30E-11	3.29E-10	0.993	3.04E+09	5.57485
26.25	4.20E-11	9.20E-12	3.11E-10	0.995	3.22E+09	7.85155
30	4.20E-11	8.05E-12	2.91E-10	0.996	3.43E+09	8.97627
33.75	4.20E-11	9.67E-12	2.75E-10	0.996	3.64E+09	7.47311
37.5	4.20E-11	2.40E-12	2.72E-10	0.99	3.68E+09	30.10417
41.25	4.20E-11	2.39E-12	2.59E-10	0.98	3.86E+09	30.23013
45	4.20E-11	3.99E-12	2.49E-10	0.995	4.02E+09	18.10777
48.75	4.20E-11	3.63E-12	2.41E-10	0.98	4.15E+09	19.90358
52.5	4.20E-11	7.68E-12	2.33E-10	0.98	4.29E+09	9.40755
54	4.20E-11	7.56E-12	2.30E-10	0.994	4.35E+09	9.55688

CHAPTER 4

CONCLUSION

This thesis provides a novel method for decreasing the surface leakage current of an infrared detector. The surface-GR dark current component is suppressed via applying a constant E-field through an insulating layer to the surface of the detector – a similar approach to MOS Field-Effect Transistors where the channel formation is controlled with applied surface-gate biasing voltage. On the contrary to the typical strong inversion operation of MOSFETs, channel formation is restrained via applying a constant electric field to form an accumulation layer on the surface.

Lattice-matched InGaAs SWIR photodetectors are commonly used in SWIR photodetector technologies. Planar type InGaAs SWIR detectors are widely used in various applications because the maturity of InGaAs technology provides the ultimate performance for a SWIR application with a cut-off wavelength of 1.69 μm. A lattice-matched InGaAs grown on an InP substrate is processed to prove the proposed concept. Rather than achieving the ultimate performance, this thesis focused on the feasibility of the proposed structure.

Mesa etched photodetector is investigated by employing the common metrics in this field. It is observed that the dark current of the photodetector improved as high as 3 times at the 300 K temperature with introducing surface-gate biasing. Additionally, the dark current of the photodetector is observed to be 4 times smaller than the zero-biased surface-gate case at the mild room temperature, comparing figures 3.16 and 3.17 at -0.1 V. The source of this improvement is investigated with dark current modeling. The methodology for this modeling is explained previously, and the reported improvement determined to be in the GR and shunt components of the dark current.

More than 90% of the GR current is suppressed at 300 K. Additionally; GR current is decreased to insignificant levels; even the inclusion of the GR current parameter became redundant at the mild room temperature measurements. Relatively more minor improvements (by a factor of 2) are reported for the shunt component of the dark current. The effect of this mechanism is said to have little to no effect on the diffusion component of the dark current; also, the photocurrent of the photodetector is observed to be not affected by surface-gate biasing. Slight improvement on the other figure of merits is also investigated, and it is found that the differential resistance of the photodetector is increased by a factor of 3 at a relatively lower reverse bias. Assuming that the detector noise is limited with the Johnson and shot noise, the specific detectivity is estimated in table 3.1. This result means improvement of the specific detectivity due to improvements in the total dark current and the differential resistance.

Overall, the expected results overlap with the experimental results as the source of the dark current is the GR current and the expected resistance improvement with the literature. This approach could also be useful for other photodetector structures such as nBn and depletion passivation [51-54], which could be utilized in combination with a variety of fields such as integrated photonics [55-58] and optomechanics [59-61].

The viability of the proposed solution is also important. In order to implement this technique to an FPA, applied surface-gate bias should be in the range of typical ROIC supply voltages. The applied surface-gate bias is inversely proportional to the insulator thickness. Thus, the given thickness of 800 nm insulating layer is the biggest obstacle to achieving a good enough improvement for FPA-ROIC coupled detectors. The thickness of the insulating layer can easily be decreased via coating or depositing various types of insulators with lower thickness. In this sense, this obstacle seems not a big issue at all. On the other hand, to reach the state-of-the-art level of performance, insulator layer should be optimized, the processing of the photodetector should be made more cautiously.

The obtained performance of the SWIR InGaAs photodetectors in literature has reached a somewhat saturation level. This method might push the performance of the mesa type photodetectors detectors by decreasing the GR current. This method can be adopted to dual-color InGaAs SWIR detectors and various other types of detectors, which can better utilize of the performance by a higher margin. Adopting this method for the extended SWIR photodetectors may result in more penetrating extended SWIR photodetectors to the market.

REFERENCES

[1] S. C. Liew, “Electromagnetic Waves,” Centre for Remote Imaging, Sensing and Processing, 2006.

[2] W. Zhien, M. Massimo, “Challenges and Opportunities in Lidar Remote Sensing,” Frontiers in Remote Sensing vol. 2, p. 3, 2021.

[3] Vial, Laurent & Chorier, P. & Gravrand, O.. “Latest results of SOFRADIR MCT technology for space applications,” Proceedings of SPIE - The International Society for Optical Engineering, vol. 7106, 2008, doi:10.1117/12.801075.

[4] M. Rowan-Robinson, “Night Vision: Exploring the Infrared Universe,” Cambridge University Press, p. 23, 2013, ISBN 1107024765.

[5] W. J. Smith, “Modern Optical Engineering,” McGraw-Hill, pp. 228-256, 2007.

[6] J. Agassi, “The Kirchhoff-Planck Radiation Law,” Science, vol. 156, no. 3771, pp. 30-37, 1967, doi:10.1126/science.156.3771.30.

[7] Rybicki, Lightman, “Radiative Processes in Astrophysics,” Wiley, pp. 20–28, 2004, ISBN 0-471-82759-2.

[8] A. Pais, “Einstein and the Quantum Theory,” Reviews of Modern Physics 51 (4), p. 863-914, 1979.

[9] A. Rogalski, K. Chrzanowski, “Infrared devices and techniques,” Optoelectronics Review, vol. 10, no. 2, pp. 111-136, 2002.

[10] W. Vereecken, U. Van Bogget, T. Colin, R.-M. Vinelli, J. Das, P. Merken, and J. Vermeiren, “A Low Noise, Extended Dynamic Range 1.3 Megapixel InGaAs Array,” Proc. SPIE - Infrared Technol. Appl. XXXIX, vol. 8704, p. 870404, 2013.

[11] G. Ghione, “Semiconductor Devices for High-Speed Optoelectronics,” Cambridge: Cambridge University Press, pp. 169, 2009, doi:10.1017/CBO9780511635595.

[12] H. Nyquist, “Thermal Agitation of Electric Charge in Conductors,” Phys. Rev., vol. 32, pp. 110-113, 1928, doi:10.1103/PhysRev.32.110.

[13] E. Milotti, “1/f Noise: A pedagogical review,” Arxiv: Physics, 2002.

[14] M. P. Hansen, D. S. Malchow, “Overview of SWIR Detectors, Cameras, and Applications,” Proc. SPIE - Thermosense XXX, vol. 6939, p. 69390I, 2008.

[15] B. Rauscher, R. Arendt, D. Fixsen, M. Greenhouse, M. Lander, D. Lindler, M. Loose, S. Moseley, D. Mott, Y. Went, D. Wilson, C. Xenophontos, “Improved Reference Sampling and Subtraction: A Technique for Reducing the Read Noise of Near-infrared Detector Systems,” Publications of the Astronomical Society of the Pacific, pp. 129, 2017, doi:10.1088/1538-3873/aa83fd.

[16] Z. Jia-Xin, W. Wei, L. Zai-Bo, Y. Hai-Feng, H. Run-Yu, H. Ze-Peng, Z. Hui, Z. Hong-xia, L. Chen, Y. Xue-Yan, S. Yan-Li, “Development of a High Performance 1280×1024 InGaAs SWIR FPA Detector at Room Temperature,” Frontiers in Physics, vol. 9, pp. 584, 2021, doi: 10.3389/fphy.2021.678192.

[17] M. Macdougal, A. Hood, J. Geske, J. Wang, F. Patel, D. Follman, J. Manzo, and J. Getty, “InGaAs Focal Plan Arrays for Low-light-level SWIR Imaging,” Proc. SPIE - Infrared Technol. Appl. XXXVII, vol. 8012, p. 83530A, 2012.

[18] G. Richard, Z. Thomas, S. Hans, “Group IV Direct Band Gap Photonics: Methods, Challenges, and Opportunities,” Frontiers in Materials, vol. 2, pp. 52, 2015, doi: 10.3389/fmats.2015.00052

[19] I. Aberg, B. Ackland, J. V Beach, C. Godek, R. Johnson, C. A. King, A. Lattes, J. O. Neill, S. Pappas, T. S. Sriram, C. S. Rafferty, N. V. Corporation, and E. Drive, “A Low Dark Current and High Quantum Efficiency Monolithic Germanium-on-Silicon CMOS Imager Technology for Day and Night Imaging Applications,” IEE Proc. - Int. Electron Devices Meet. IEDM, vol. 978, no. 1, pp. 344–347, 2010.

[20] I. Tamm, “A possible kind of electron binding on crystal surfaces. Physikalische Zeitschrift der Sowjetunion,” vol. 1, p. 733-746, 1932.

[21] J. Chu, A. Sher, “Device Physics of Narrow Gap Semiconductors,” Springer New York, pp.189-192, 2007, doi:10.1007/978-1-4419-1040-0.

[22] W. Shockley, W.T. Read, “Statistics of the recombinations of holes and electrons,” Phys Rev 87, pp. 835-842, 1952.

[23] W. Gräfe, “Extension of the surface recombination model and unique determination of the recombination energy by means of reverse current measurements,” Phys Status Solidi A, vol. 4, pp. 655-662, 1971.

[24] Y.J. Chung, R. Villegas, K.A. Baldwin, K.W. et al, “Ultra-high-quality two-dimensional electron systems,” Nat. Mater., vol. 20, pp. 632–637, 2021, doi: 10.1038/s41563-021-00942-3

[25] A. Daniels, “Field Guide to Infrared Systems, Detectors, and FPAs, 3rd Edition” SPIE, pp. 102-118, 2018, doi: 10.1117/3.2315935.ch83

[26] G. R. Savich, “Analysis and Suppression of Dark Currents in Mid-Wave Infrared Photodetectors by,” University of Rochester, 2015.

[27] B. T. Marozas, W. D. Hughes, X. Du, D. E. Sidor, G. R. Savich, and G. W. Wicks, “Surface dark current mechanisms in III-V infrared photodetectors [Invited],” Opt. Mater. Express, vol. 8, no. 6, p. 1419, 2018, doi: 10.1364/ome.8.001419.

[28] R. G. Driggers, V. Hodgkin, and R. Vollmerhausen, “What Good is SWIR? Passive Day Comparison of VIS, NIR, and SWIR,” Proc. SPIE - Infrared Imaging Syst. Des. Anal. Model. Test. XXIV, vol. 8706, p. 87060L, 2013.

[29] A. Rogalski, “Infrared Detectors (2nd ed.),” CRC Press, pp. 366-382, 2010, doi.org/10.1201/b10319.

[30] P. Martyniuk, A. Rogalski, “HOT infrared photodetectors,” Opto-Electronics Review, vol. 21, 2013, doi:10.2478/s11772-013-0090-x.

[31] H. Figgemeier, M. Benecke, K. Hofmann, R. Oelmaier, A. Sieck, J. Wendler, J. Ziegler, “SWIR detectors for night vision at AIM,” Proc. SPIE 9070, Infrared Technology and Applications XL, 907008, 2014, doi.org/10.1117/12.2050320.

[32] F. Rutz, P. Kleinow, R. Aidam, W. Bronner, L. Kirste, M. Walther, “InGaAs infrared detector development for SWIR imaging applications,” Proc SPIE 8896, 2013, doi:10.1117/12.2026879.

[33] K. H. Goetz, D. Bimberg, H. Jürgensen, J. Selders, A. V. Solomonov, G. F. Glinskii, M. Razeghi, (1983). “OPTICAL AND CRYSTALLOGRAPHIC PROPERTIES AND IMPURITY INCORPORATION OF GaxIn1 - xAs (0. 44 less than x less than 0. 49) GROWN BY LIQUID PHASE EPITAXY, VAPOR PHASE EPITAXY AND METAL ORGANIC CHEMICAL VAPOR DEPOSITION,” Journal of Applied Physics 54(8), p. 4543-4552, 1983, doi.org/10.1063/1.332655

[34] S. Adachi, “Physical properties of III-V semiconductor compounds: InP, InAs, GaAs, GaP, InGaAs, and InGaAsP,” New York: Wiley, pp. 17-192, 1992, doi.org/10.1002/352760281X.

[35] P. Sajal, J. B. Roy, P. K. Basu, “Empirical expressions for the alloy composition and temperature dependence of the band gap and intrinsic carrier density in GaxIn1−xAs,” Journal of Applied Physics 69, p. 827-829, 1991, doi.org/10.1063/1.348919.

[36] M. A. Littlejohn, K. W. Kim, and H. Tian, “High-field transport in InGaAs and related heterostructures, Properties of Lattice-matched and strained indium gallium arsenide,” P. Bhattacharya (INSPEC), 1993.

[37] K. Somogyi and J. Pfeifer, “Electron mobility measured in undoped InGaAs epitaxial layer grown on n-InP substrate,” Appl. Phys. Lett. 61, p. 2220-2221, 1992, doi.org/10.1063/1.108273.

[38] L. Södergren, N. S. Garigapati, M. Borg, and E. Lind, “Mobility of near surface MOVPE grown InGaAs/InP quantum wells,” Appl. Phys. Lett. 117, 013102, 2020, doi.org/10.1063/5.0006530.

[39] C. Kittel, “Introduction to Solid State Physics 6th Edition,” John Wiley & Sons, Inc. New York, pp. 185, 1986.

[40] D. Strauch, U. Rössler, “InP: lattice parameters, Landolt-Börnstein - Group III Condensed Matter 44D (New Data and Updates for IV-IV, III-V, II-VI and I-VII Compounds, their Mixed Crystals and Diluted Magnetic Semiconductors),” SpringerMaterials, 2011, doi: 10.1007/978-3-642-14148-5_285.

[41] D. N. Bose, “Properties, processing and applications of indium phosphide,” Circuits and Devices Magazine, IEEE. vol. 17. p. 34-35, 2001, doi:10.1109/MCD.2001.950059.

[42] J. Zhang, W. Wang, Z. Li, H. Ye, R. Huang, Z. Hou, H. Zeng, H. Zhu, C. Liu, X. Yang, Y. Shi, (2021). “Development of a High Performance 1280×1024 InGaAs SWIR FPA Detector at Room Temperature,” Frontiers in Physics. 9, 678192, 2021, doi:10.3389/fphy.2021.678192.

[43] X. Li, X. M. Shao, T. Li, ZC. Cheng, Z. C. Huang, S. L. Huang, et al, “Research Progress of Short Wave Infrared InGaAs Focal Plane Detectors,” Infrared Laser Engineering, vol. 01, p. 64–71, 2020, doi:10.3788/IRLA202049.0103006.

[44] R. Fraenkel, E. Berkowicz, L. Bykov, R. Dobromislin, R. Elishkov, A. Giladi, et al, “High Definition 10μm Pitch in Ga as Detector with Asynchronous Laser Pulse Detection Mode,” Proceedings of the Infrared Technology & Applications XLII, 2016, doi:10.1117/12.2222762.

[45] M. Macdougal, J. Geske, C. Wang, S. Liao, J. Getty, A. Holmes, “Low Dark Current in Ga as Detector Arrays for Night Vision and Astronomy,” Proceedings of the Infrared Technology & Applications XXXV, May 2009, doi:10.1117/12.820377.

[46] A. D. Hood, M. H. Macdouga, D. Follman, J. Manzo, J. C. Geske, “Large-format InGaAs Focal Plane Arrays for SWIR Imaging,” Infrared Technology and Applications XXXVIII, Proceedings vol. 8353, May 2012, doi:10.1117/12.921475.

[47] P. P. Dixon, C. Li, M. Ettenberg, C. D. Hess, J. Trezza, “Dual-band Technology on Indium Gallium Arsenide Focal Plane Arrays,” Proceedings of SPIE – The International Society for Optical Engineering, p. 150–4, 2011, doi:10.1117/12.883412.

[48] P. Yuan, J. C. Boisvert, N. Karam, “Low-dark Current 1024x1280 InGaAs PIN Arrays,” Proceedings of the Infrared Technology & Applications XLInternational Society for Optics and Photonics, June 2014, doi:10.1117/12.2053999.

[49] C. Hu, “Modern semiconductor devices for integrated circuits,” Upper Saddle River, N.J: Prentice Hall, pp. 157-175, 2010.

[50] M. E. Law, E. Solley, M. Liang and D. E. Burk, “Self-consistent model of minority-carrier lifetime, diffusion length, and mobility,” IEEE Electron Device Letters, vol. 12, no. 8, pp. 401-403, 1991, doi: 10.1109/55.119145.

[51] F. Uzgur, and S. Kocaman, “Barrier engineering for HgCdTe unipolar detectors on alternative substrates,” Infrared Physics & Technology vol. 97, pp. 123-128, 2019.

[52] K. Circir, M. H. Dolas, and S. Kocaman, “Optimization of in-device depleted passivation layer for InGaAs photodetectors,” Infrared Physics & Technology vol. 97, pp. 360-364, 2019.

[53] M. H. Halit, and S. Kocaman, “Fully depleted InP nano-layer for in-device passivation of InGaAs SWIR detectors,” IEEE Electron Device Letters vol. 38, no. 12, pp. 1692-1695, 2017.

[54] F. Uzgur et al. “All InGaAs unipolar barrier infrared detectors,” IEEE Transactions on Electron Devices vol. 65, no. 4, pp. 1397-1403, 2018.

[55] S. Kocaman, et al. “Zero phase delay in negative-refractive-index photonic crystal superlattices,” Nature Photonics vol. 5, no. 8, pp. 499-505, 2011.

[56] A, Govdeli, et al. “Integrated optical modulator based on transition between photonic bands,” Scientific reports vol. 8, no .1, pp. 1-11, 2018.

[57] M. Shahram, A. Govdeli and S. Kocaman, “Zero average index design via perturbation of hexagonal photonic crystal lattice,” Optical Materials vol. 73, pp. 577-584, 2017.

[58] S. Kocaman, et al. “On-chip optical filters with designable characteristics based on an interferometer with embedded silicon photonic structures,” Optics Letters vol. 37, no .4, pp. 665-667, 2012.

[59] Y. Ozer, and S. Kocaman, “Stability formulation for integrated opto-mechanic phase shifters,” Scientific reports vol. 8, no .1, pp. 1-9, 2018.

[60] M. Erdil, Y. Ozer, and S. Kocaman, “High-Q slot-mode photonic crystal nanobeam cavity biosensor with optomechanically enhanced sensitivity,” IEEE Journal of Selected Topics in Quantum Electronics vol. 25, no .2, pp. 1-6, 2018.

[61] O. E. Orsel, M. Erdil, and S. Kocaman, “A 2D slotted rod type PhC cavity inertial sensor design for impact sensing,” IEEE Journal of Quantum Electronics vol. 56, no .1, pp. 1-8, 2019.